PROCEEDINGS A

royalsocietypublishing.org/journal/rspa

Research



Cite this article: Al Ba'ba'a H, Nouh M, Singh T. 2019 Dispersion and topological characteristics of permutative polyatomic phononic crystals. *Proc. R. Soc. A* **475**: 20190022. http://dx.doi.org/10.1098/rspa.2019.0022

Received: 14 January 2019 Accepted: 20 May 2019

Subject Areas:

wave motion, mechanics, acoustics

Keywords:

phononic crystal, band gap, permutations

Author for correspondence:

M. Nouh

e-mail: mnouh@buffalo.edu

Electronic supplementary material is available online at https://doi.org/10.6084/m9.figshare. c.4553972.

THE ROYAL SOCIETY PUBLISHING

Dispersion and topological characteristics of permutative polyatomic phononic crystals

H. Al Ba'ba'a, M. Nouh and T. Singh

Department of Mechanical and Aerospace Engineering, University at Buffalo (SUNY), Buffalo, NY 14260-4400, USA

HA, 0000-0003-3805-6002; MN, 0000-0002-2135-5391; TS, 0000-0003-0377-6122

This work presents a comprehensive mathematical treatment of phononic crystals (PCs) which comprise a finite lattice of repeated polyatomic unit cells. Wave dispersion in polyatomic lattices is susceptible to changes in the local arrangement of the monatoms (subcells) constituting the individual unit cell. We derive and interpret conditions leading to identical and contrasting band structures as well as the possibility of distinct eigenmodes as a result of cyclic and non-cyclic cellular permutations. Different modes associated with cyclic permutations yield topological invariance, which is assessed via the winding number of the complex eigenmode. Wave topology variations in the polyatomic PCs are quantified and conditions required to support edge modes in such lattices are established. Next, a transfer function analysis of finite polyatomic PCs is used to explain the formation of multiple Bragg band gaps as well as the emergence of truncation resonances within them. Anomalies arising from the truncation of the infinite lattice are further exploited to design mirror symmetrical edge modes in an extended lattice. We conclude with a generalized explanation of the band gap evolution mechanism based on the Bode plot analysis.

1. Introduction

Phononic crystals (PCs) are artificially engineered structures constructed from a periodic arrangement of materials in single [1] or multiple directions [2,3]. PCs are a realization of an array of identical unit cells which, as a result of their periodic arrangement, enable a rich domain of unconventional mechanical properties with applications in vibroacoustic mitigation [4], focusing [5], flow control [6] and acoustic topological insulators [7]. Of specific interest to this work is the ability of PCs to exhibit unique wave dispersion properties culminating

in the formation of phononic band gaps, which are symptomatic of their ability to impede vibrations within extended frequency ranges [8]. Band gaps in non-dissipative PCs are commonly explained in light of Bragg scattering and impedance mismatches resulting from their periodic architecture. This ability to spatially attenuate waves without resorting to rubber-like or soft viscoelastic polymers places PCs in a unique position to impact applications in need of structural and acoustic damping without compromising their load-bearing ability. In addition to PCs, other classes of phononic materials have recently gained traction by including alternative or supplemental attenuation and/or band gap enhancement mechanisms including, but not limited to, locally resonant metamaterials [3,9], inertially amplified structures [10,11] and negative capacitance piezo-shunts [12]. In their most common configuration, PCs are perceived as a one-dimensional two-layered periodic material that undergoes axial excitation resulting in longitudinal elastic waves [13]. In its idealized form, a lattice of two distinct spring-mass systems represents the individual unit cell of such diatomic PC which, over the past decade, has been at the heart of recent developments in the domains of nonlinear wave guides [14–17], topological edge states [18] and in breaking wave reciprocity to realize diode-like acoustic structures [19,20].

For wave dispersion analysis, PCs are mathematically treated as spatially infinite periodic medium [21]. While effective for band structure calculations (e.g. via Bloch-wave and Floquet methods), this assumption is physically unrealistic. It fails to capture the effects of both: (i) the number of cells in the finite arrangement and (ii) the terminal boundary conditions on the PC's actual response. It is also critical to note that the desired wave manipulation capabilities, often sought in phononic or locally resonant systems, do not necessarily materialize in finite (i.e. truncated) realizations with limited number of individual unit cells. Examples of discrepancies include formation of resonances inside the band gap, and undeveloped band gaps in terms of attenuation strength and/or width [22]. Hence, understanding the initiation and evolution of the dynamic properties (such as band gaps) of finite PCs is non-trivial and has recently warranted a different approach [23–25].

The focus of this work is a generalized class of higher-order phononic lattices structured from repeated polyatomic unit cells [26-29]. Polyatomic PCs are idealized counterparts of elastic multi-layered periodic composites [30], the dynamics of which are modelled as periodic continuants which appear in numerous physics and engineering applications [31]. Given the added complexity of such higher-dimension systems, performance analysis means are often based on numerical simulations and approximated methods. As a result, analytical closed-form solutions which lend insights into the behaviour of finite polyatomic phononic lattices and provide correlations between dispersion predictions and their actual response remains lacking. The primary goal of this effort is, therefore, to fill this gap and, in the process, enable us to: (1) Derive analytical expressions to determine band gap maximum attenuation and sonic speed of an equivalent continuum model. (2) Examine the effect of different permutations of the constitutive subcells on: (i) emergent band structures and (ii) eigenvectors (modes) at the band gap limits. The latter is used to explain, in a coherent manner, intriguing wave phenomena arising in diatomic lattices (which is a special subset of the polyatomic PCs) such as 'band inversion', 'mirror symmetry' and 'edge modes', which are vital for topologically protected systems [32,33]. We compute and use the winding number of the complex eigenvector associated with the dispersion relation to quantify the different topological features of such lattices [34]. Finally, we conclude our study with a generalized Bode plot analysis to help understand the underlying formation mechanisms of Bragg band gaps in higher-order systems as well as the possibility of truncation resonances within such gaps.

2. Wave dispersion

(a) Mathematical formulation

Consider an infinite chain of a polyatomic PC with a unit cell comprising \mathcal{E} different masses and stiffnesses as shown in figure 1. The equation of motion of the ξ th mass in the cell is

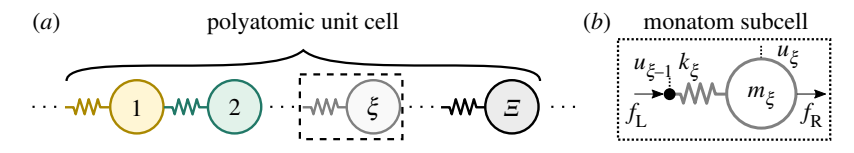


Figure 1. Unit cell of a polyatomic phononic crystal (*a*) and free body diagram of an individual monatom (*b*). (Online version in colour.)

given by

$$m_{\xi}\ddot{u}_{\xi} + (k_{\xi} + k_{\xi+1})u_{\xi} - k_{\xi}u_{\xi-1} - k_{\xi+1}u_{\xi+1} = 0.$$
 (2.1)

The periodicity of the PC mandates that $k_{\xi+\Xi}=k_{\xi}$ and, similarly, $m_{\xi+\Xi}=m_{\xi}$ where $\xi=1,2,\ldots,\Xi$. By virtue of the spatial periodicity, implementing the Bloch-wave theorem is possible and the displacements of the unit cell ends are related. Hence, we write $u_0=u_{\Xi}e^{-i\hat{\beta}}$ and $u_{\Xi+1}=u_1e^{i\hat{\beta}}$, where $\hat{\beta}$ is the dimensionless wavenumber and $i=\sqrt{-1}$ denotes the imaginary unit. Upon condensing the displacements using the previous conditions, the complete set of equations governing the motion of the entire unit cell can be written in the compact matrix form:

$$\mathbf{M}_{c}\ddot{\mathbf{u}}_{c}(t) + \mathbf{K}_{c}(\bar{\beta})\mathbf{u}_{c}(t) = \mathbf{0}, \tag{2.2}$$

where (") = (d^2/dt^2) denotes the second derivative in time t and

$$\mathbf{u}_{c}(t) = \begin{cases} u_{1}(t) & u_{2}(t) & \dots & u_{E}(t) \end{cases}^{\mathrm{T}}, \tag{2.3a}$$

$$\mathbf{M}_{\mathbf{c}} = \mathbf{diag} \Big[m_1, m_2, \dots, m_{\mathcal{Z}} \Big]$$
 (2.3b)

and

$$\mathbf{K}_{\mathbf{c}}(\bar{\beta}) = \begin{bmatrix} k_1 + k_2 & -k_2 & 0 & \dots & 0 & -k_1 e^{-i\bar{\beta}} \\ -k_2 & k_2 + k_3 & -k_3 & 0 & \dots & 0 \\ 0 & -k_3 & \ddots & \ddots & \ddots & \vdots \\ \vdots & \ddots & \ddots & \ddots & \ddots & 0 \\ 0 & \dots & 0 & \ddots & \ddots & -k_{\Xi} \\ -k_1 e^{i\bar{\beta}} & 0 & \dots & 0 & -k_{\Xi} & k_{\Xi} + k_1 \end{bmatrix}$$
 (2.3c)

Assuming a harmonic solution $\mathbf{u}_c(t) = \hat{\mathbf{u}}_c(\omega) \mathrm{e}^{\mathrm{i}\omega t}$, the dynamic stiffness matrix $\mathbf{D}_c(\bar{\beta},\omega) = [\mathbf{K}_c(\bar{\beta}) - \omega^2 \mathbf{M}_c]$ can be found and equation (2.2) is reduced to $\mathbf{D}_c(\bar{\beta},\omega)\hat{\mathbf{u}}_c(\omega) = \mathbf{0}$. The dispersion relation can be found by setting the determinant of \mathbf{D}_c equal to zero (henceforth, we use $\mathbf{D}_c \equiv \mathbf{D}_c(\bar{\beta},\omega)$ for brevity). Now, let us define a matrix that is based on the tridiagonal part of the matrix \mathbf{D}_c (as if $\mathrm{e}^{\mathrm{i}\bar{\beta}} = \mathrm{e}^{-\mathrm{i}\bar{\beta}} = 0$) which is denoted here by $\bar{\mathbf{D}}_c$. Next, we denote $\Delta_{i,j} = |\bar{\mathbf{D}}_c(i:j,i:j)|$ as the determinant of the main minor of the matrix $\bar{\mathbf{D}}_c$ constructed from the rows and columns spanning i to j, such that $j \geq i$. Making use of the linear property of expanding a matrix's determinant into a sum of two determinants (For more details, see [35,36]), it can be shown that

$$|\mathbf{D}_c| = \Delta_{1,\Xi} - k_1^2 \Delta_{2,\Xi-1} - 2\kappa \cos(\bar{\beta}), \tag{2.4}$$

where $\kappa = k_1 k_2 \dots k_{\Xi}$. For the special case of $i \ge j$, the determinant $\Delta_{i,j}$ yields different values as follows [37]:

$$\Delta_{i,j} = \begin{cases} 0 & j < i - 1 \\ 1 & j = i - 1 \\ d_i & j = i \end{cases}$$
 (2.5)

where $d_i = (k_{i+1} + k_i - m_i \omega^2)$ are the diagonal elements of \mathbf{D}_c . To obtain an explicit form of the determinant $|\mathbf{D}_c|$ in equation (2.4), an expression for $\Delta_{i,j}$ is derived. To facilitate the analysis, we

factor out a diagonal matrix $C_{i,j}$ from $\Delta_{i,j}$ as follows:

$$\Delta_{i,j} = \underbrace{\begin{vmatrix} c_i & & & \\ & c_{i+1} & & \\ & & \ddots & \\ & & & c_{j} \end{vmatrix}}_{C_{i,j}} \underbrace{\begin{vmatrix} \frac{d_i}{c_i} & -\frac{k_{i+1}}{c_i} & & \\ -\frac{k_{i+1}}{c_{i+1}} & \ddots & \ddots & \\ & & \ddots & \ddots & -\frac{k_j}{c_{j-1}} \\ & & & -\frac{k_j}{c_j} & \frac{d_j}{c_j} \end{vmatrix}}_{\bar{\Delta}_{i,i}}, \tag{2.6}$$

such that the opposing off-diagonal elements of $\bar{\Delta}_{i,j}$ have the product of 1. The entries c_i are defined as

$$c_{i} = \begin{cases} \frac{k_{2}k_{4} \dots k_{\Xi-1}}{k_{3}k_{5} \dots k_{\Xi}} & i = 1\\ k_{2} \frac{k_{3}k_{5} \dots k_{\Xi}}{k_{4}k_{6} \dots k_{\Xi-1}} & i = 2\\ k_{i} \frac{k_{3}k_{5} \dots k_{i-2}}{k_{2}k_{4} \dots k_{i-1}} \frac{k_{i+1}k_{i+3} \dots k_{\Xi-1}}{k_{i+2}k_{i+4} \dots k_{\Xi}} & \text{mod}(i, 2) \neq 0, i \neq 1\\ k_{i} \frac{k_{2}k_{4} \dots k_{i-2}}{k_{3}k_{5} \dots k_{i-1}} \frac{k_{i+2}k_{i+4} \dots k_{\Xi}}{k_{i+1}k_{i+3} \dots k_{\Xi-1}} & \text{mod}(i, 2) = 0, i \neq 2 \end{cases}$$

$$(2.7)$$

for odd Ξ , and

$$c_{i} = \begin{cases} \frac{k_{2}k_{4} \dots k_{\Xi}}{k_{3}k_{5} \dots k_{\Xi-1}} & i = 1\\ k_{2} \frac{k_{3}k_{5} \dots k_{\Xi-1}}{k_{4}k_{6} \dots k_{\Xi}} & i = 2\\ k_{i} \frac{k_{3}k_{5} \dots k_{i-2}}{k_{2}k_{4} \dots k_{i-1}} \frac{k_{i+1}k_{i+3} \dots k_{\Xi}}{k_{i+2}k_{i+4} \dots k_{\Xi-1}} & \text{mod}(i, 2) \neq 0, i \neq 1\\ k_{i} \frac{k_{2}k_{4} \dots k_{i-2}}{k_{3}k_{5} \dots k_{i-1}} \frac{k_{i+2}k_{i+4} \dots k_{\Xi}}{k_{i+4} \dots k_{\Xi}} & \text{mod}(i, 2) = 0, i \neq 2 \end{cases}$$

$$(2.8)$$

for an even \mathcal{Z} , respectively. Here, the 'mod' function denotes the modulo operator. An interesting feature of tridiagonal matrices is that two tridiagonal matrices have an equivalent determinant if their diagonals are identical and the product of each opposing off-diagonal elements gives matching values [37]. As such, $\bar{\Delta}_{i,j}$ is equivalent to the following determinant:

$$\bar{\Delta}_{i,j} = \begin{vmatrix} \bar{d}_i & 1 \\ 1 & \ddots & \ddots \\ & \ddots & \ddots & 1 \\ & 1 & \bar{d}_j \end{vmatrix}, \tag{2.9}$$

where $\bar{d}_i = \frac{m_i}{c_i}(\omega_i^2 - \omega^2)$ and $\omega_i^2 = (k_i + k_{i+1})/m_i$ and the structure of the matrix is analogous to that of a simple continuant with its determinant $\bar{\Delta}_{i,j}$ being a function of the diagonal elements only [38]. By increasing the order of the matrix and observing the pattern of $\bar{\Delta}_{i,j}$, a generalized equation for such determinant can be deduced. The equation is found to be a successive summation of the product of the following terms:

$$\bar{\Delta}_{i,j} = \sum_{\bar{\xi}} (-1)^{\frac{\bar{z}-\bar{\xi}}{2}} \sum_{i_1} \sum_{i_2} \dots \sum_{i_{\bar{\xi}}} \bar{d}_{i_1} \bar{d}_{i_2} \dots \bar{d}_{i_{\bar{\xi}}} + (-1)^{\frac{\bar{z}}{2}} \delta_{\text{mod}(\bar{z},2),0}, \tag{2.10}$$

where $\delta_{\mathrm{mod}(\bar{\mathcal{Z}},2),0}$ is the Kronecker delta, $\bar{\mathcal{Z}}=j-i+1$ is the order of the matrix minor and $\bar{\xi}=1,3,\ldots,\bar{\mathcal{Z}}$ or $\bar{\xi}=2,4,\ldots,\bar{\mathcal{Z}}$ for odd and even \mathcal{Z} , respectively. The summation indices are

$$i_1 = i, i + 2, \dots, j - \bar{\xi} + 1$$
 (2.11a)

$$i_2 = i_1 + 1, i_1 + 3, \dots, j - \bar{\xi} + 2$$
 (2.11b)

:

$$i_{\bar{\xi}} = i_{\bar{\xi}-1} + 1, i_{\bar{\xi}-1} + 3, \dots, j - \bar{\xi} + \bar{\xi}.$$
 (2.11c)

Examples of the indices combinations are provided in the supplementary material. Based on the determinant $\bar{\Delta}_{i,j}$ and the expansion of the $d_{i_1}d_{i_2}\dots d_{i_\xi}$ terms in equation (2.10), the closed-form expression of the dispersion relation for a polyatomic PC comprising \mathcal{Z} monatomic subcells can be derived as

$$2\varkappa \Big(1 - \cos(\bar{\beta})\Big) + \sum_{\xi=1}^{\mathcal{Z}} (-1)^{\xi} \alpha_{\xi} \omega^{2\xi} = 0.$$
 (2.12)

It is worth noting that, as clearly observed in equation (2.12), the expression α_0 always reduces to $2\varkappa$, which is in line with the findings of [26,27] and $\alpha_\xi=\alpha_\xi^{1,\mathfrak{F}}-k_1^2\alpha_\xi^{2,\mathfrak{F}-1}$, where

$$\alpha_{\xi}^{i,j} = |\mathbf{C}_{i,j}| \sum_{\bar{\xi} > \xi} (-1)^{(\bar{\mathcal{E}} - \bar{\xi}/2)} \sum_{i_1} \dots \sum_{i_{\bar{\xi}}} \sum_{i_r = 1}^{\bar{r}} \frac{m_{i_1} \dots m_{i_{\bar{\xi}}}}{c_{i_1} \dots c_{i_{\bar{\xi}}}} \left(\prod_{\hat{r} \in \mathbf{r}_{i_r}} \omega_{\hat{r}}^2 (1 - \delta_{(\bar{\xi} - \xi),0}) + \delta_{(\bar{\xi} - \xi),0} \right)$$
(2.13)

such that $\bar{r} = \begin{pmatrix} \bar{\xi} \\ \hat{\varepsilon} \end{pmatrix}$ and

$$\begin{bmatrix} \mathbf{r}_1 \\ \mathbf{r}_2 \\ \vdots \\ \mathbf{r}_{\bar{r}} \end{bmatrix} = \begin{pmatrix} i_1, i_2, \dots, i_{\bar{\xi}} \\ \bar{\xi} - \xi \end{pmatrix}. \tag{2.14}$$

Solving equation (2.12) over the range $\bar{\beta} \in [0, \pi]$ —also known as the irreducible Brillouin zone (IBZ)—results in Ξ dispersion branches (bands) and provides the free-wave solution of the dispersion equation. Once the coefficients of the dispersion relation are determined, the driven-wave solution, where the wavenumber is found as a function of the excitation frequency $\bar{\beta}(\omega) = \cos^{-1}(\Phi(\omega))$, can be cast as

$$\Phi(\omega) = 1 + \frac{1}{\alpha_0} \sum_{\xi=1}^{\mathcal{Z}} (-1)^{\xi} \alpha_{\xi} \omega^{2\xi}.$$
 (2.15)

(b) Band gap attenuation extrema

Within a band gap, the wavenumber $\bar{\beta}$ is complex and its imaginary component dictates the rate of attenuation of the wave's spatial profile in its propagation direction. The complex component of the wavenumber is often obtained from the driven-wave problem, i.e. equation (2.15), which represents a system undergoing an excitation which has a prescribed frequency. To find the frequencies corresponding to the utmost wave attenuation within a set of band gaps (attention extrema), the derivative of $\Phi(\omega)$ with respect to ω is evaluated and is equated to zero

$$\frac{d\Phi(\omega)}{d\omega} = \frac{2}{\alpha_0} \sum_{\xi=1}^{\mathcal{Z}} (-1)^{\xi} \xi \alpha_{\xi} \omega^{2\xi-1} = 0, \tag{2.16}$$

which can be simplified as

$$\frac{d\Phi(\omega)}{d\omega} = \sum_{k=1}^{\Xi} (-1)^{k} \xi \alpha_{\xi} \omega^{2(k-1)} = 0, \tag{2.17}$$

such that it includes non-zero solutions of ω . The roots of equation (2.17) return the frequency of maximum attenuation within a band gap and are, therefore, expressed as ω_{max} . We substitute these roots back into equation (2.15) and then into $\bar{\beta}(\omega_{\text{max}}) = \cos^{-1}(\Phi(\omega_{\text{max}}))$ to find the maximum attenuation constant $\Im[\bar{\beta}(\omega_{\text{max}})]$ corresponding to ω_{max} [8]. The number of bounded band gaps exhibited by a polyatomic PC is one short of the number of dispersion branches, i.e. $(\mathcal{Z}-1)$, and, hence, there exists an equivalent number of $(\omega_{\text{max}}, \Im[\bar{\beta}(\omega_{\text{max}})])$ pairs.

(c) Sonic speed

The sonic speed c_s of a lattice represents the initial slope of the acoustic branch of the dispersion relation, which symbolizes the propagation speed of a wave packet (i.e. group velocity) in the elastic medium at the long wavelength limit. An identical c_s is conventionally employed as a baseline to compare the dissipative performance of different classes of phononic materials [39]. Two different periodic structures with matching sonic speeds (i.e. initial dispersion slope) are said to possess static equivalence. Here, an analytical derivation of the sonic speed of the polyatomic PC is presented. To find the desired slope, we evaluate the derivative of equation (2.12) with respect to $\bar{\beta}$:

$$\varkappa \sin(\bar{\beta}) + \frac{\partial \omega}{\partial \bar{\beta}} \sum_{k=1}^{\Xi} (-1)^{\xi} \xi \alpha_{\xi} \omega^{2\xi - 1} = 0.$$
 (2.18)

In the vicinity of $\bar{\beta}=0$, the dispersion relation can be assumed linear and the phase velocity approaches the group velocity, i.e. $(\partial \omega/\partial \bar{\beta}) \approx (\omega/\bar{\beta})$. Given that at $\bar{\beta} \approx 0$, ω is also infinitesimal and, therefore, all higher-order terms of ω can be neglected. Considering $\xi=1$ only and applying the previous assumptions with $\sin(\bar{\beta}) \approx \bar{\beta}$, equation (2.18) now reads

$$\kappa - \alpha_1 \left(\frac{\partial \omega}{\partial \bar{B}}\right)^2 = 0. \tag{2.19}$$

Rearranging the previous equation and applying $c_s = (\partial \omega / \partial \bar{\beta})$ gives

$$c_{\rm S} = \frac{\partial \omega}{\partial \bar{\beta}} = \sqrt{\frac{\varkappa}{\alpha_1}},\tag{2.20}$$

where α_1 is given by

$$\alpha_1 = \sum_{\xi=1}^{\mathcal{Z}} m_{\xi} \left(\sum_{\xi=1}^{\mathcal{Z}} k_{\xi} k_{\xi+1} \dots k_{\xi+\mathcal{Z}-2} \right).$$
 (2.21)

The second term in equation (2.21) can be found by adding the product of $\mathcal{Z}-1$ subgroups of the vector $[k_1, k_2, \dots, k_{\mathcal{Z}}]$, i.e.:

$$\begin{pmatrix} k_1, k_2, \dots, k_{\Xi} \\ \Xi - 1 \end{pmatrix} . \tag{2.22}$$

The order of the vector $[k_1, k_2, ..., k_{\Xi}]$ does not influence the outcome of equation (2.22) which implies that adding the product of the resulting subgroups is indifferent to the arrangement of the elements in $[k_1, k_2, ..., k_{\Xi}]$. This leads to the conclusion that all possible arrangements of material properties within a polyatomic unit cell exhibit identical sonic speeds at the long wave speed limit.

(d) Effect of subcell (monatom) arrangement

For the simple diatomic PC, changing the order of the material properties, i.e. 1-2 or 2-1, does not influence the final dispersion relation [18]. On the other hand, the dispersion relation of a higher-order polyatomic PC ($\mathcal{E} > 2$) is susceptible to changes in the subcell arrangement. As such, it is of interest to examine the possible dispersion outcomes associated with various combinations of subcell orders. As an illustrative example, and without loss of generality, we consider the

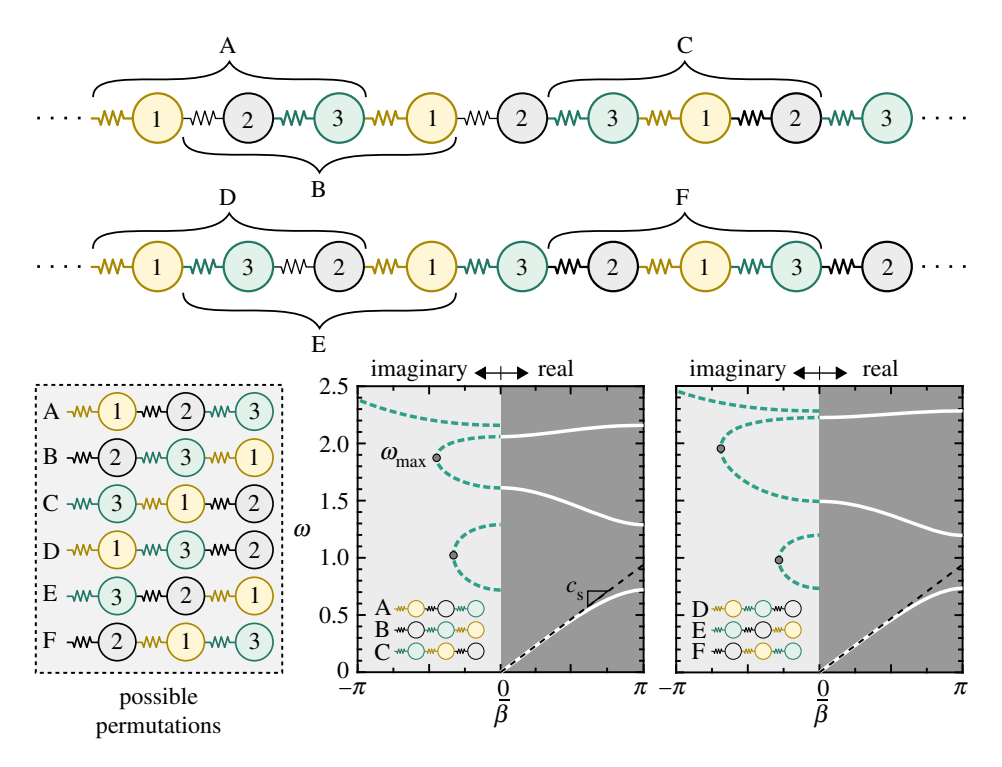


Figure 2. Possible permutations of a triatomic PC (A through F) and their corresponding dispersion diagrams. Solid and dashed lines denote the real and imaginary components of the non-dimensional wavenumber $\bar{\beta}$, respectively. Labels for c_s (sonic speed) and ω_{max} (frequency of maximum attenuation) are marked on both diagrams. (Online version in colour.)

dispersion characteristics of a triatomic PC with all possible permutations of its constitutive monatoms. Figure 2 shows all of the combinations and their respective dispersion relations for $m_1 = k_1 = 1$, $m_2 = k_2 = 2$ and $m_3 = k_3 = 3$. We notice that the triatomic PC can be configured in six different permutations which yield only two distinctive band structures. The permutations that share identical dispersion relations are found to be cyclic, for instance, the groups A,B and C in figure 2.

As explained earlier, the sonic speed is immune to the cellular arrangement, although the band gap widths change significantly as can be seen in figure 2, a fact that is pivotal in the design stages. In other words, when limited to a particular set (database) of materials, choosing a specific permutation is primarily contingent on the design requirement. It is important to note here that some permutations may initially seem as reciprocals of each other, but, in truth, they yield different dispersion relations (e.g. 1–3–2 and 2–3–1). This property is characteristic of lumped spring-mass systems where, contrast to continuous phononic bars/beams, the reciprocal configurations do not mirror each other. Specifically, the arrangement 1–3–2 is defined by the sequence $k_1-m_1-k_3-m_3-k_2-m_2$ while 2–3–1 corresponds to $k_2-m_2-k_3-m_3-k_1-m_1$. If we consider m_3 as an example, the first case shows that it is connected with k_2 and k_3 unlike the second case, where it is coupled with k_1 and k_3 . Each of these cases results in a different dynamic matrix yielding distinct dispersion relations as a consequence, an effect that disappears when the masses are identical, or with alike springs and different masses. A systematic proof of the invariance of the dispersion relation under cyclic permutations using the transfer matrix method (TMM) is detailed in the supplementary material.

Based on the discussion above, a generalization of the number of distinct band structures of a polyatomic PC can be stated as follows: for a unit cell with \mathcal{E} different materials (i.e. different masses and stiffnesses), there exists $(\mathcal{E}-1)!$ sets of distinct dispersion diagrams and for the

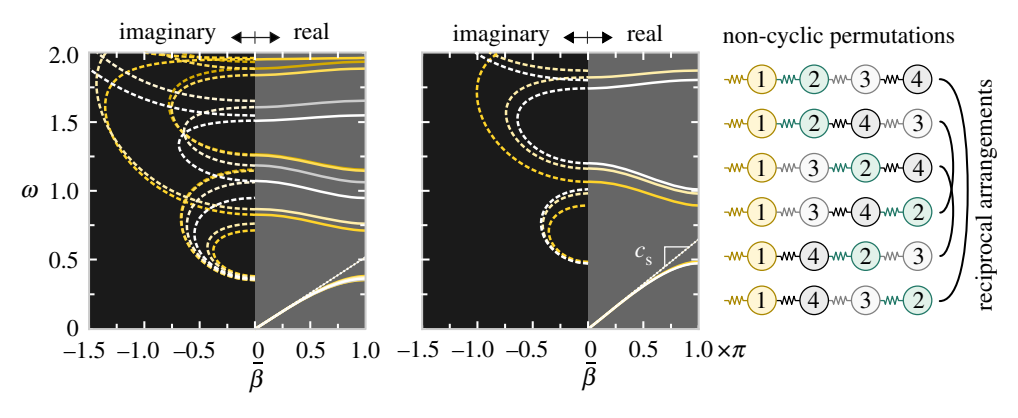


Figure 3. Dispersion diagrams up to $\omega=2$ for a tetratomic PC for $k_1=1$, $k_2=2$, $k_3=3$ and $k_4=1/4$. Unit cell masses are chosen as follows: $m_1=1$, $m_2=2$, $m_3=3$ and $m_4=1/4$ (left), $m_1=m_2=m_3=m_4=1$ (right). Six distinct band structures exist for the arrangement on the left (non-identical masses) compared to only three for the one on the right (identical masses). The non-cyclic permutations used to produce the dispersion diagram are displayed for reference. The reciprocal unit cell arrangements yield the same dispersion diagram when masses are equal. (Online version in colour.)

cases with equal values of masses or stiffnesses, the number of distinct sets is halved. Figure 3 shows two cases of a tetratomic lattice: the first consists of distinct masses and stiffnesses, while the second comprises uniform masses but dissimilar spring constants. The tetratomic lattice (i.e. $\mathcal{E}=4$) exhibits 24 permutations with $(\mathcal{E}-1)!=6$ distinct dispersion diagrams for the first case, while the number of diagrams is halved for the second case as a result of the identical masses. The reason being that these non-cyclic permutations are reciprocals of one another and can be deduced from a deliberate selection of the unit cell. For an extended tetratomic PC of the sequence 1–2–3–4–1–2–3–4..., the unit cell can be selected from left-to-right or right-to-left, which, for instance, yields the permutations 1–2–3–4 and 1–4–3–2 when spring 1 is set as a starting point.

(e) Eigenvectors at band gap limits

An important aspect to highlight regarding cyclic permutations is the behaviour of the eigenvectors at the edges of a given band gap, a criterion which has lately garnered considerable attention in the domains of topological edge states and insulators in periodic acoustic and mechanical systems [40,41]. The limits of a band gap are found from the solution of the dispersion relation (i.e. the eigenvalues of \mathbf{D}_c) at the boundaries of the IBZ, i.e. $\bar{\beta} = 0, \pi$. To derive the corresponding eigenvector, we set the displacement amplitude of the last mass to unity, i.e. $\hat{u}_{\Xi} = 1$, and compute relative amplitudes of the rest of the displacement field using:

$$\hat{u}_{\xi-1} = \frac{k_{\xi}}{D_{\xi-1}} \hat{u}_{\xi} \pm \frac{k_1 k_2 \dots k_{\xi-1}}{D_1 D_2 \dots D_{\xi-1}},\tag{2.23}$$

where + and - represent $\bar{\beta} = 0$ and $\bar{\beta} = \pi$, respectively. The D terms are derived based on the Gaussian elimination of the reduced eigenvalues problem with the substitution of an eigenvalue and is given by the following general formula:

$$D_{\xi+1} = d_{\xi+1} - \frac{k_{\xi+1}^2}{D_{\xi}} = d_{\xi+1} - \frac{k_{\xi+1}^2}{d_{\xi} - (k_{\xi}^2/(d_{\xi-1} - (k_{\xi-1}^2/\dot{\cdot}\cdot)))},$$
(2.24)

which is analogous to the computation of a continuous fraction [42]. Note that D_1 is equal to d_1 . For a set of cyclic permutations, it suffices to compute the eigenpairs for one of them. While the

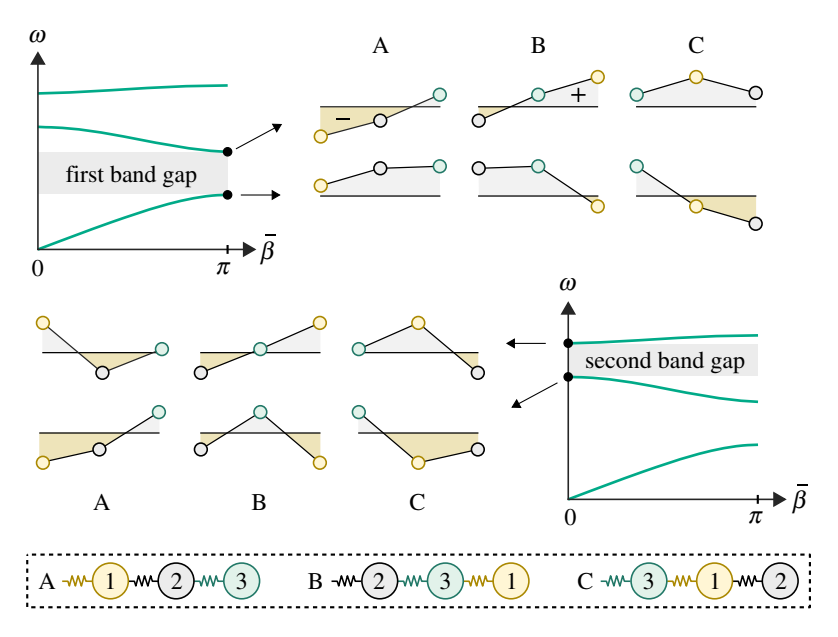


Figure 4. Mode shapes of one group of the cyclic permutations of the triatomic PC displayed in figure 2, namely: A, B and C, at the edges of both the first and second band gaps. (Online version in colour.)

eigenvalues of cyclic permutations remain unchanged, the eigenvectors are, however, unique and found by applying a permutation matrix **P** to the computed eigenvector, which reads

$$\mathbf{P}_{\Xi \times \Xi} = \begin{bmatrix} \mathbf{0} & \mathbf{I}_{\Xi - 1} \\ \pm 1 & \mathbf{0} \end{bmatrix},$$
(2.25)

where \pm conditions are identical to that of equation (2.23). For example, if we start with the permutation $1-2-\ldots-\mathcal{E}$, then multiplying the eigenvector with the permutation matrix \mathbf{P} once produces a new eigenvector that belongs to the permutation $2-3-\ldots-\mathcal{E}-1$. The proposed technique for computing the eigenvectors for cyclic permutations is, however, valid for combinations of spring constants and masses that render the matrix \mathbf{D}_c a spectrum with unrepeated entities (i.e. an indefective \mathbf{D}_c matrix). Given a specific eigenvalue, if all corresponding eigenvectors from the different cyclic permutations are cast into one matrix, denoted here as \mathbf{U} , the following pattern is observed:

$$\mathbf{U}_{\Xi \times \Xi} = \begin{bmatrix} \hat{\mathbf{u}}_c & \mathbf{P}\hat{\mathbf{u}}_c & \dots & \mathbf{P}^{\Xi - 2}\hat{\mathbf{u}}_c & \mathbf{P}^{\Xi - 1}\hat{\mathbf{u}}_c \end{bmatrix}. \tag{2.26}$$

Figure 4 shows the eigenvectors (mode shapes) of the different triatomic PC permutations, namely: A, B and C, at the edges of both band gaps. In the case of the first gap, the sign of the permuting mass changes with every sequence but its amplitude is preserved. For the second gap, a similar behaviour is observed albeit without the sign change, as evident from the permutation matrix **P**. Alternatively, the results obtained from the permutation matrix **P** can be also deduced from the phase shift between neighbouring unit cells. Based on Bloch boundary conditions, the displacement of the ξ th mass of the ith unit cell is related to its peer in the adjacent (i+1)th cell via $u_{\mathcal{Z}+\xi}=u_{\xi}\mathrm{e}^{\mathrm{i}\vec{\beta}}$. That is, the unit cells as a block flip signs if the band gap is sandwiched between two limits at $\vec{\beta}=\pi$ while preserve their sign when the band gap is sandwiched between two limits at $\vec{\beta}=0$. If the cyclic permutations are selected from the two successive unit cells as illustrated in figure 5 (shown for the upper limit of both gaps in figure 4), the same behaviour concluded from the permutation matrix **P** in equation (2.25) and displayed in figure 4 is recovered. The concept of the permutation matrix **P** shown here serves as an elementary proof for the

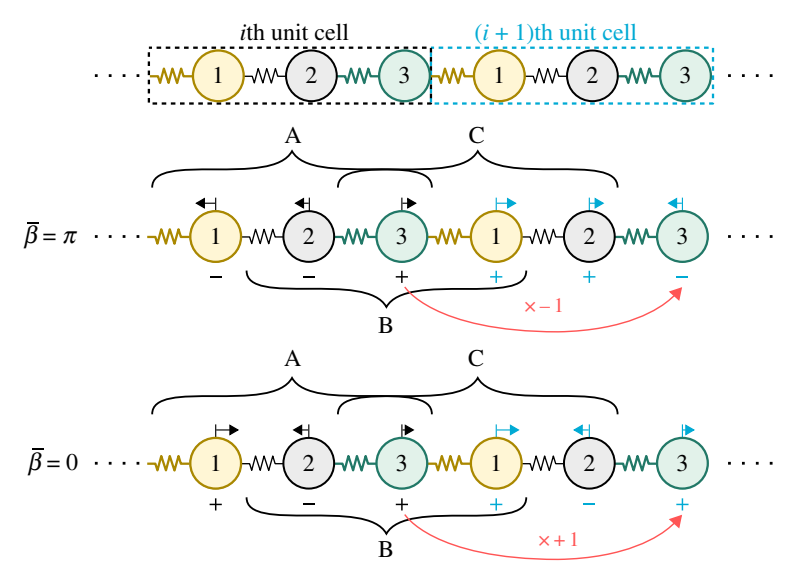


Figure 5. Illustrative schematic of the eigenvectors (mode shapes) of two neighbouring unit cells at the upper limit of the first and second band gaps in figure 4, corresponding to $\bar{\beta} = \pi$ and $\bar{\beta} = 0$, respectively. (Online version in colour.)

'band inversion' phenomenon reported in diatomic PC lattice [18,34]. Conventionally, in-phase oscillations typically reside in the acoustic branch while out-of-phase oscillations occur in the optic branch. Band inversion refers to a situation where in-phase and out-of-phase modes switch places at the limits of the band gap between the acoustic and optic branches following cyclic permutations. Starting with the eigenvectors at the band gap limits: $\mathbf{u}_c^1 = \{1, 1\}^T$ and $\mathbf{u}_c^2 = \{-1, 1\}^T$ for a diatomic lattice with unequal stiffnesses and identical masses, the permutation matrix (with a negative sign) can be applied to produce $\mathbf{v}_c^1 = \mathbf{P}\mathbf{u}_c^1 = \{1, -1\}^T \equiv \{-1, 1\}^T$ and $\mathbf{v}_c^2 = \mathbf{P}\mathbf{u}_c^2 = \{-1, -1\}^T \equiv \{1, 1\}^T$, corresponding to the eigenvectors of the cyclic permutation.

(f) Topological aspects of polyatomic phononic crystals

It is now established that polyatomic lattices with cyclic cellular permutations share identical band structures (i.e. eigenvalues) but non-matching eigenvectors, a feature which motivates an investigation of their topological properties. The Zak phase is a well-known metric in wave topology that distinguishes between different unit cell candidates which have a distinct band structure [18,43]. Normalizing the Zak phase by a unit of π leads to the winding number ν of the eigenvector around the origin of the complex plane (we refer the reader to current literature for more on the calculation of ν [34,44]). As a starting point, consider a triatomic lattice with equal masses and one different spring per unit cell, as shown in figure 6a. The motivation behind this choice will become clear shortly. The cyclic permutations of such arrangement, shown in figure 6a, expectedly generate an identical band structure. However, only one permutation possesses an integer value of ν , which is non-zero for $k_1 > k_2$ (figure 6b). This permutation exhibits mirror symmetry about the spring separating two successive unit cells. In other words, cells on each side of the mirror (within the dashed boundaries) are reciprocal arrangements of one another. If more than one spring is allowed to be different, the mirror symmetry condition cannot be satisfied and ν will not be *quantized*, i.e. the associated system can no longer be topologically protected. It is worth noting that the fact that the Zak phase is not always quantized (implying that ν is not an integer by necessity) and its dependence on unit cell symmetry has been noted in the literature [43]. Further, a correction factor has also been suggested to sustain the integer nature (in π units) of the Zak phase [45].

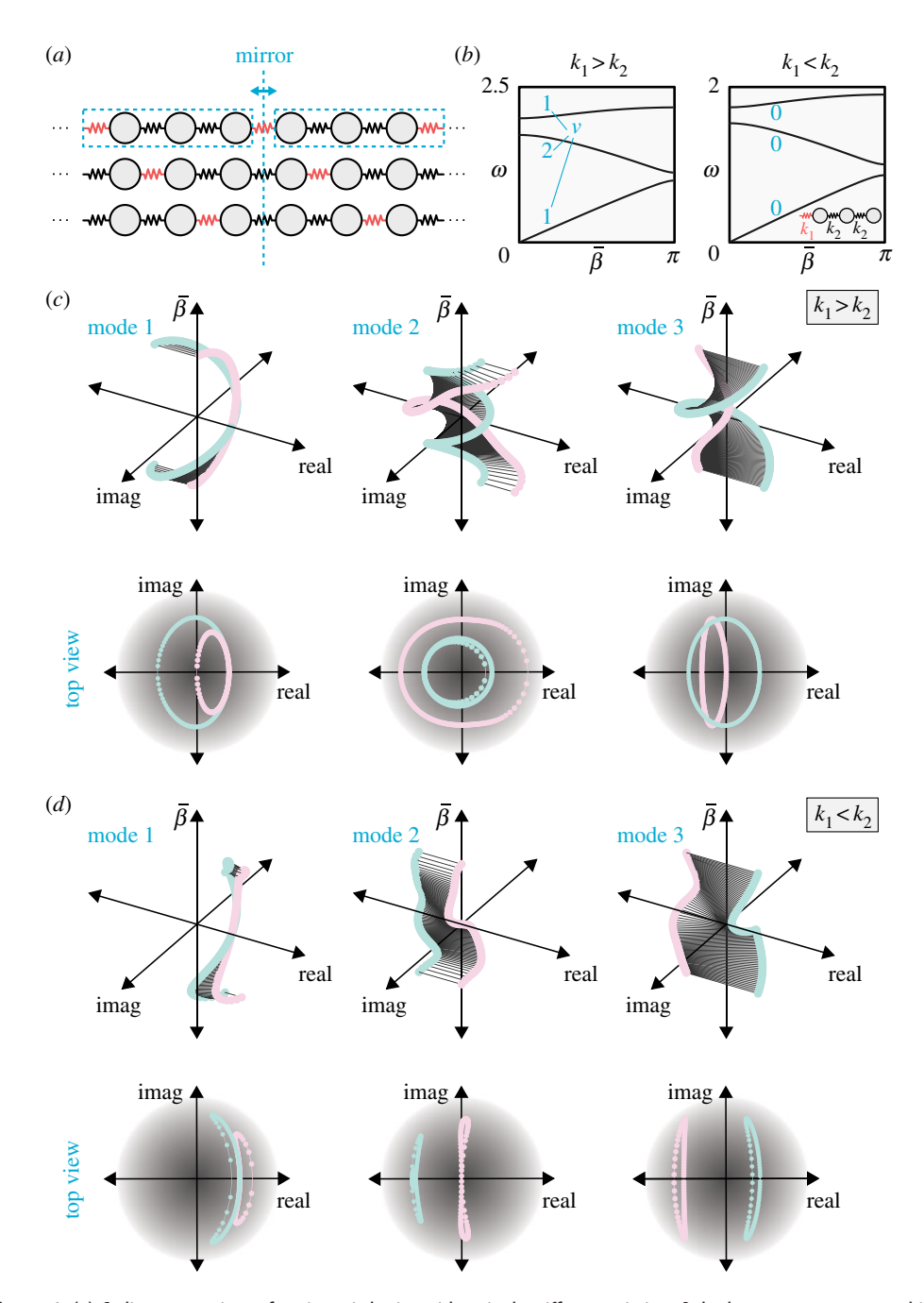


Figure 6. (a) Cyclic permutations of a triatomic lattice with a single stiffness variation. Only the top arrangement exhibits mirror unit cell symmetry. (b) Dispersion diagram for the mirror symmetric permutation for $k_1 > k_2$ and $k_1 < k_2$; the winding number ν associated with each band is indicated. (c,d) Variation of the complex mode shapes as a function of the dimensionless wavenumber $\bar{\beta}$ for $k_1 > k_2$ and $k_1 < k_2$. The line connecting the two complex components of the mode shapes encircles the origin only for modes corresponding to $k_1 > k_2$. In the shown simulations, $(k_2/k_1) = (3/2)$ and (2/3). (Online version in colour.)

As indicated earlier, ν quantifies the number of times an eigenvector winds around the origin of the complex plane. In a diatomic PC, the eigenvector may be normalized such that one component remains real while the other is complex and, therefore, the rotation about the origin can be unambiguously illustrated in the complex plane. For the triatomic case, on the other hand,

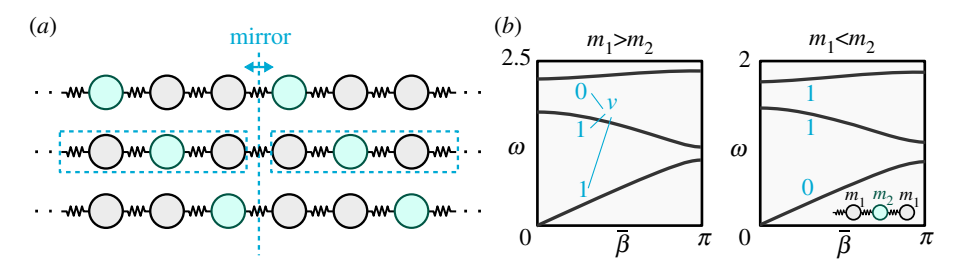


Figure 7. (*a*) Cyclic permutations of a triatomic lattice with identical springs and varying masses. (*b*) Winding numbers ν associated with the dispersion branches of the $m_1-m_2-m_3$ unit cell for $m_1>m_2$ and $m_1< m_2$. (Online version in colour.)

the eigenvector is three-dimensional and normalizing the first to be real leaves two complex components. The winding of the eigenvector in this scenario can be visualized by the rotation of a line connecting the two complex components as a function of the wavenumber $\bar{\beta}$. This is graphically depicted in figure 6c and d for $k_1 > k_2$ and $k_1 < k_2$, respectively. The eigenvector does not encircle the origin for $k_1 < k_2$ and, hence ν is zero. For $k_1 > k_2$, it winds around the origin once for the first and third modes and twice for the second mode. Unlike the diatomic PC, a unique ν may not be assigned to the entire lattice. Instead, it is defined for individual bands when E > 2 as evident by the unequal values of ν when $k_1 > k_2$. Visualizing the eigenvector rotation around the origin for higher-order hierarchies of the polyatomic PC might not be as straightforward. For a tetratomic PC, as a case in point, this may be visualized as the winding of an area connecting three complex components of the eigenvector around the origin. For higher-order lattices, it becomes a difficult exercise in imagination. Mirror symmetry in polyatomic PCs with E > 2 is not limited to polyatomic lattices with identical masses, and can be generalized to configurations with different masses and identical springs. Such generalization is not feasible for diatomic PCs [34]. An illustrative schematic and an example of this case are displayed in figure 7.

A closing of the band gap is an indispensable condition to obtain two lattices with topologically invariant metrics. The examples provided in figures 6 and 7 satisfy this condition at $k_1 = k_2$ and $m_1 = m_2$, respectively. In other words, the gap closes and opens again as we transition from $k_1 > k_2$ (or $m_1 > m_2$) to $k_1 < k_2$ (or $m_1 < m_2$), changing the winding number ν as a result. As the number of monatoms comprising the polyatomic unit cell grows, the possible combinations of springs (or masses) that forces at least one band gap to close also increases. The reason being that, in polyatomic PCs, a higher number of variations within a unit cell remains possible without violating the mirror symmetry requirement. In fact, $(\Xi - 1)/2$ springs (or masses) in a unit cell with an odd number of monatoms are allowed to be different. For example, for a triatomic cell (i.e. $\mathcal{Z}=3$), this shown by the sole 'red' spring in figure 6a. As long as one of the cyclic permutations of the unit cell is symmetric, e.g. the $k_1 - k_2 - k_1$, then there exists one permutation among this group that satisfies mirror symmetry and, consequently, yields an integer winding number ν . In the case of varying masses and identical springs, as shown in figure 7, the symmetric unit cell configuration (i.e. $m_1 - m_2 - m_1$) automatically guarantees such mirror symmetry. The aforementioned criteria do not extend to unit cells with an even number of monatoms where more than one arrangement can satisfy mirror symmetry within one cycle of permutations.

To attain a clear picture of topological variations in polyatomic lattices, we exploit barycentric coordinates as a means to construct a map of the ν values corresponding to various combinations of lattice properties. We limit the analysis here to polyatomic lattices with identical masses and modulated springs, while maintaining the mirror symmetry condition. In the barycentric space, a constraint is specified between the variables of interest and every possible combination thereof is swept within the constrained space. In the top row of figure 8, for example, the stiffnesses k_1 and k_2 of a triatomic lattice (figure 6) are swept by a line (1-simplex) such that $(k_1 + k_2)$ is equal to a constant k and the resultant ν is indicated. The lines are colour-coded such that segments sharing the same ν also share the same colour. The coordinates along the line are (k_1, k_2) and the

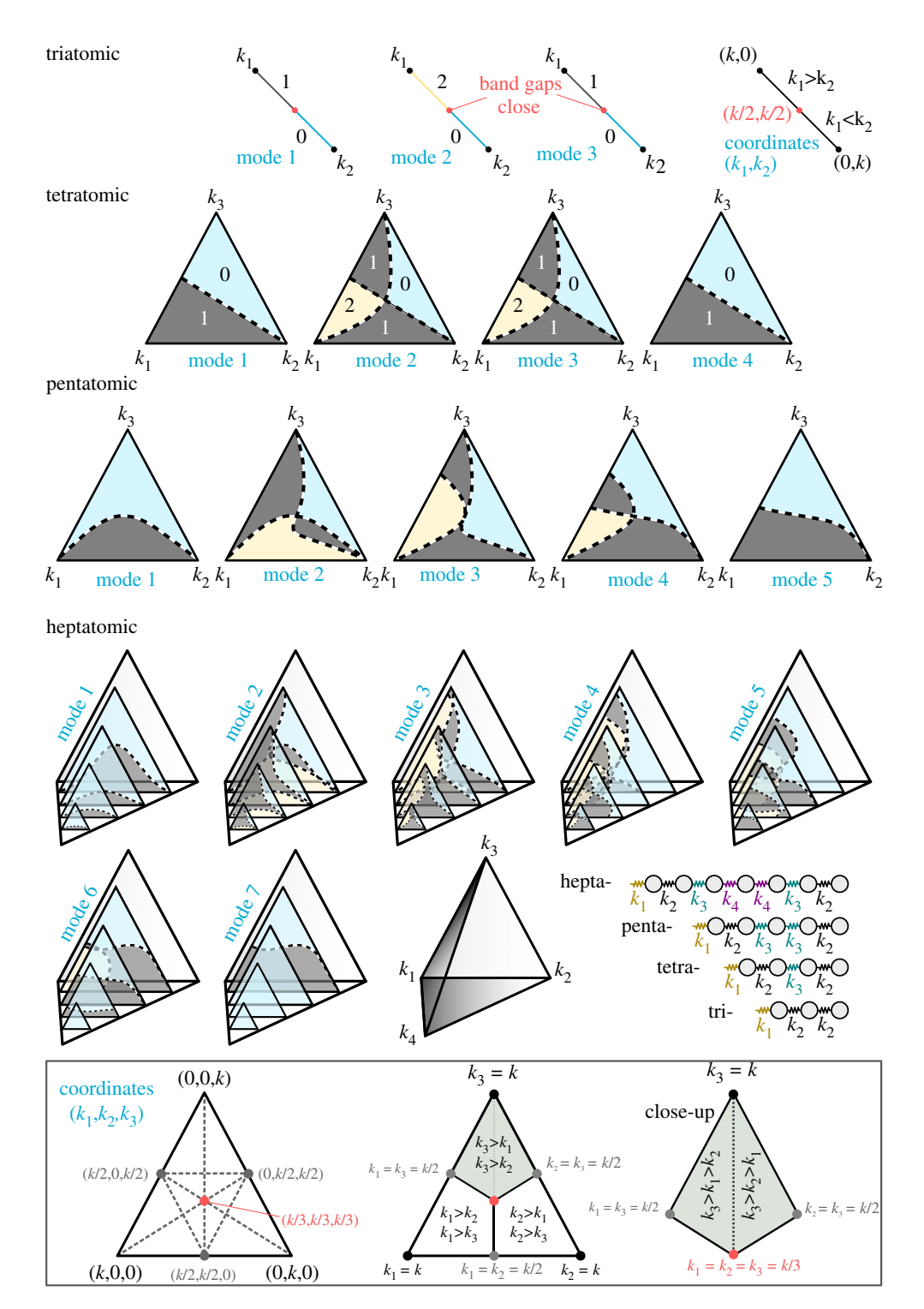


Figure 8. Winding numbers associated with different stiffness combinations in tri-, tetra-, penta- and heptatomic lattices, demonstrated via the barycentric coordinates. The barycentric geometry depends on the number of variables and is graphically represented with a line, triangle and tetrahedron for two (triatomic), three (tetratomic/pentatomic) and four (heptatomic) stiffness variables, respectively. The dashed border lines indicate band gap closings and separate regions with a different winding number ν . The regions are colour-coded to signal the value of ν . The bottom panel provides a detailed guide for the triangular barycentric space for reference. (Online version in colour.)

midpoint corresponds to $k_1 = k_2 = (k/2)$, where the band gaps close. The two vertices, i.e. (k,0)and (0,k), are labelled as k_1 and k_2 to emphasize the dominance of one variable relative to the other as we approach a vertex. The ratio between the variables becomes either zero or infinity at each of the two vertices (e.g. $(k_1/k_2) = (k/0) = \infty$ at the k_1 vertex). Extending the analysis to three variables is similar in concept with the constraint being $k_1 + k_2 + k_3 = k$. As such, the barycentric space becomes a triangle (2-simplex) as in the cases of the tetratomic and pentatomic unit cells depicted in the second and third rows of figure 8. The dashed lines separate the various ν regions (shaded using the same colour codes) and a detailed description of the different combinations of k_1 , k_2 and k_3 is provided in the key at the bottom of the figure. It is important to note that moving along the edges of the triangle dictates that one of the spring constants is zero, which is physically unrealistic. Hence, the values obtained at the edges are excluded and the spanned space is infinitesimally smaller than the barycentric triangle. For a heptatomic lattice with four stiffness variables, the domain of barycentric coordinates extends to a tetrahadron (3-simplex). Once again, the dashed border lines separate the various ν regions and correspond to band gap closings. Every border line is shared between two neighbouring modes and moving along it closes the band gap sandwiched between these modes. Consequently, if a common border line does not exist between two modes, then the sandwiched band gap remains open for all considered combinations and, as a result, v remains unaltered. Beyond heptatomic lattices, the corresponding simplex will encounter a larger number of vertices and will permit a similar, albeit more complex, analysis to be conducted.

3. Structural dynamics of a finite polyatomic phononic crystal lattice

(a) Equations of motion

The equations of motion of a finite polyatomic PC give rise to a class of matrices known as periodic continuant matrices [31]. The continuant matrix usually comprises a period Ξ , which denotes the number of subcells, and a number of periods (cells) *n* with a class *r* resulting in a matrix order of $N = n\Xi + r$. In particular, we are interested in cases with r = 0 (note that $r = \text{mod}(N, \Xi)$) implying that the structure has an integer number of cells (complete periods), whereas $r \neq 0$ is indicative of an incomplete last period. Hence, the dynamics of a polyatomic PC is given by

$$\mathbf{M\ddot{u}}(t) + \mathbf{K}\mathbf{u}(t) = \mathbf{f}(t), \tag{3.1}$$

where $\mathbf{M} = \mathbf{I}_n \otimes \mathbf{M}_c$ and

$$\mathbf{K}_{ij} = \begin{cases} k_{i+1} + k_i - (\epsilon \delta_{i,1} + \epsilon \delta_{i,N}) & i = j \\ -k_{\max(i,j)} & |i - j| = 1 \\ 0 & |i - j| \neq 1, 0 \end{cases}$$
(3.2a)

$$\mathbf{u}(t) = \begin{cases} \mathbf{u}_{c_1}(t) \\ \mathbf{u}_{c_2}(t) \\ \vdots \\ \mathbf{u}_{c_n}(t) \end{cases}$$
(3.2b)

$$\mathbf{f}(t) = \left\{ f(t) \quad 0 \quad \dots \quad 0 \right\}^{\mathrm{T}},\tag{3.2c}$$

and

such that \otimes is the Kronecker product, I_n is the unit matrix with size $n \times n$ and $\mathbf{u}_{c_n}(t)$ is the displacement vector of the nth unit cell. The excitation f(t) is imposed on the first mass since the interest of the current analysis is to ultimately find the end-to-end transfer function. The stiffness matrix K is generalized for a polyatomic structure with any prescribed boundary

conditions represented by the variables ϵ and ϵ . Applying the Laplace transform and introducing $D = Ms^2 + K$, we arrive at

$$\mathbf{D}(s)\mathbf{u}(s) = \mathbf{f}(s),\tag{3.3}$$

where

$$\mathbf{D}_{ij}(s) = \begin{cases} d_i(s) - (\epsilon \delta_{i,1} + \epsilon \delta_{i,N}) & i = j \\ -k_{\max(i,j)} & |i - j| = 1 \\ 0 & |i - j| \neq 1, 0. \end{cases}$$
(3.4)

(b) Transfer function

(i) System poles

The characteristic polynomial (containing the poles of the dynamical system) is derived from the determinant of the dynamic stiffness matrix in equation (3.4). Here, we start by stating the characteristic polynomial $\phi_N(\lambda)$, where λ is the eigenvalue, for an unperturbed matrix (i.e. $\epsilon = \varepsilon = 0$) which resembles a fixed-fixed lattice with general matrix size N [37]:

$$\phi_{N}(\lambda) = \varkappa^{\lfloor N/\Xi \rfloor} \left[\Delta_{1,r}(\lambda) U_{\lfloor N/\Xi \rfloor}(\nu_{\Xi}(\lambda)) + \frac{k_{2}^{2}k_{3}^{2} \dots k_{r+1}^{2}k_{1}^{2}}{\varkappa} \Delta_{r+2,\Xi-1}(\lambda) U_{\lfloor (N-\Xi)/\Xi \rfloor}(\nu_{\Xi}(\lambda)) \right], \quad (3.5)$$

where $\lfloor \cdot \rfloor$ denotes the floor function and $U_{\lfloor N/\Xi \rfloor}(\nu_{\Xi}(\lambda))$ is the Chebyshev polynomial of the second kind and its input function $\nu_{\Xi}(\lambda)$ is given by

$$\nu_{\mathcal{Z}}(\lambda) = \frac{1}{2\nu} \left(\Delta_{1,\mathcal{Z}}(\lambda) - k_1^2 \Delta_{2,\mathcal{Z}-1}(\lambda) \right). \tag{3.6}$$

Here, the term $\Delta_{i,j}$ is the *s*-domain version of equation (2.4), i.e. $s^2 = -\omega^2$. Given that $\mathbf{D}(s)$ is a perturbed matrix, we expand the first and last rows of the determinant of $\mathbf{D}(s)$ into a sum of determinants using the linear property of determinants to make use of equation (3.5). This process results in the characteristic polynomial of the perturbed $\mathbf{D}(s)$

$$\phi_N^*(\lambda) = \phi_N(\lambda) + \epsilon \bar{\phi}_{N-1}(\lambda) + \varepsilon \phi_{N-1}(\lambda) + \varepsilon \epsilon \bar{\phi}_{N-2}(\lambda), \tag{3.7}$$

where

$$\bar{\phi}_{N} = \varkappa^{\lfloor N/\Xi \rfloor} \left[\Delta_{2,r+1}(\lambda) U_{\lfloor N/\Xi \rfloor}(\nu_{\Xi}(\lambda)) + \frac{k_{3}^{2}k_{4}^{2} \dots k_{r+2}^{2}k_{2}^{2}}{\varkappa} \Delta_{r+3,\Xi}(\lambda) U_{\lfloor (N-\Xi)/\Xi \rfloor}(\nu_{\Xi}(\lambda)) \right]. \tag{3.8}$$

For brevity, we write $\phi_N(\lambda)$ henceforth as ϕ_N (and similarly for the other terms) and substitute $N = n\Xi$. Hence, each term in equation (3.7) can be written in its final form by using the definitions stated in equations (3.8) and (2.5):

$$\phi_{\Xi n} = \kappa^n U_n(\nu_{\Xi}) + \kappa^{n-1} k_1^2 \Delta_{2,\Xi - 1} U_{n-1}(\nu_{\Xi}), \tag{3.9a}$$

$$\phi_{\Xi n-1} = \kappa^{n-1} \Delta_{1,\Xi-1} U_{n-1}(\nu_{\Xi}), \tag{3.9b}$$

$$\bar{\phi}_{\Xi n-1} = \varkappa^{n-1} \Delta_{2,\Xi} U_{n-1}(\nu_{\Xi}) \tag{3.9c}$$

$$\bar{\phi}_{\Xi n-2} = \kappa^{n-1} \Delta_{2,\Xi - 1} U_{n-1}(\nu_{\Xi}) + \frac{\kappa^n}{k_1^2} U_{n-2}(\nu_{\Xi}). \tag{3.9d}$$

Note that the $k_2^2k_3^2\dots k_{r+1}^2$ becomes unity if r<1. Here, a special emphasis is placed on the free-free case of the polyatomic PC. After substituting the boundary condition values ($\epsilon=\epsilon=-k_1$ for an unconstrained PC), equation (3.7) reduces to

$$\phi_{\Xi n}^* = \varkappa^n \left[U_n(\nu_{\Xi}) + U_{n-2}(\nu_{\Xi}) - \frac{k_1}{\varkappa} \left(\Delta_{2,\Xi} + \Delta_{1,\Xi-1} - 2k_1 \Delta_{2,\Xi-1} \right) U_{n-1}(\nu_{\Xi}) \right]. \tag{3.10}$$

Knowing that $U_n(\cos(\theta)) = \sin((n+1)\theta)/\sin(\theta)$ from Chebyshev polynomial properties, equation (3.10) now reads

$$\phi_{\Xi n}^* = \frac{\kappa^n}{\sin(\theta)} \left[\sin\left((n+1)\theta\right) + \sin\left((n-1)\theta\right) - \frac{k_1}{\kappa} \left(\Delta_{2,\Xi} + \Delta_{1,\Xi-1} - 2k_1 \Delta_{2,\Xi-1}\right) \sin\left(n\theta\right) \right]. \quad (3.11)$$

Note here that setting $v_{\Xi} = \cos(\theta)$ results in equation (2.4), i.e. the dispersion relation, which governs the eigenvalues of the system with θ being the solutions of $\phi_{\Xi n}^* = 0$. With a few further manipulations and exploiting trigonometric identities, we obtain

$$\phi_{\Xi n}^* = \varkappa^{n-1} \left[2\varkappa \cos(\theta) - k_1(\Delta_{2,\Xi} + \Delta_{1,\Xi-1} - 2k_1\Delta_{2,\Xi-1}) \right] \frac{\sin(n\theta)}{\sin(\theta)}. \tag{3.12}$$

Making use of equation (3.6) and the fact that $v_{\Xi} = \cos(\theta)$ as stated earlier, we arrive at

$$\phi_{\Xi n}^* = \varkappa^{n-1} \left[\Delta_{1,\Xi} - k_1 \Delta_{2,\Xi} - k_1 \Delta_{1,\Xi - 1} + k_1^2 \Delta_{2,\Xi - 1} \right] \frac{\sin(n\theta)}{\sin(\theta)}. \tag{3.13}$$

From equation (3.7), it can be shown that

$$\Delta_{1,\Xi}^* = \Delta_{1,\Xi} - k_1 \Delta_{2,\Xi} - k_1 \Delta_{1,\Xi-1} + k_1^2 \Delta_{2,\Xi-1}$$
 (3.14)

is the determinant of the matrix $\bar{\mathbf{D}}_c$ with a perturbation value of $\epsilon = \varepsilon = -k_1$ (i.e. single unconstrained unit cell) and, therefore, the characteristic polynomial of the perturbed $\mathbf{D}(s)$ is written as

$$\phi_{\Xi n}^* = \kappa^{n-1} \Delta_{1,\Xi}^* \frac{\sin(n\theta)}{\sin(\theta)}.$$
 (3.15)

Setting the characteristic polynomial in equation (3.15) equal to zero yields the solutions of $\theta_{\ell} = (\ell \pi / n)$, for $\ell = 1, 2, ..., n-1$ and the corresponding eigenvalues are found from the roots of the following polynomial:

$$P(s) = \Delta_{1,\Xi}^* \prod_{\ell=1}^{n-1} \left(\sum_{\xi=1}^{\Xi} \alpha_{\xi} s^{2\xi} + 2\varkappa \left(1 - \cos(\theta_{\ell}) \right) \right). \tag{3.16}$$

The second term in equation (3.16) is the *s*-domain version of the dispersion relation in equation (2.12), which means that the roots of equation (3.16) satisfy the dispersion relation and lie on one of the dispersion branches. As a result, θ_ℓ can be seen as a discretized form of the wavenumber. Furthermore, the lattice's natural frequencies correspond to the dispersion relation roots at such discrete points [8]. The first term $\Delta_{1,\mathcal{E}}^*$, on the other hand, represents what are often denoted as *truncation poles*. Its roots do not necessarily satisfy the dispersion relation and, consequently, often appear inside the band gap. The presented analysis can be extended to other boundary conditions, i.e. other values of ε and ε (for a comprehensive list of other possible boundary conditions, refer to [8]). However, an explicit solution of θ_ℓ is not always guaranteed.

(ii) System zeros

Unlike the system poles in equation (3.16), the zeros polynomial Z(s) of the dynamical system is established based on the desired actuation and sensing locations (i.e. the input and output). The structure of the tridiagonal matrix describing the dynamics of the polyatomic lattice, i.e. $\mathbf{D}(s)$, allows the determination of the zeros of the transfer function using the determinant of a minor of the matrix $\mathbf{D}(s)$. For the specific case of the end-to-end transfer function, the matrix of interest is a minor of $\mathbf{D}(s)$ constructed by deleting the first row (corresponding to the excitation location) and the last column (corresponding to the sensing location) and its determinant can

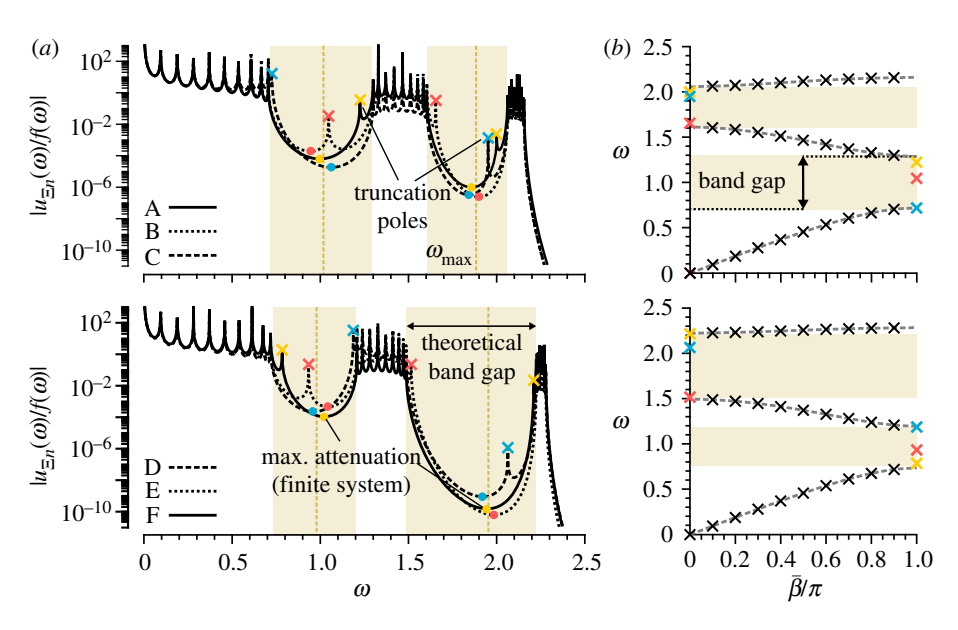


Figure 9. (a) Frequency response functions (FRFs) of a triatomic PC with n=10 cells for all possible unit cell permutations: A through F in figure 2. (b) Corresponding distribution of natural frequencies of the finite PC (marked as cross symbols) projected on the band structure obtained for an infinite system. Numerically obtained maximum attenuations in the FRF are marked as circles and the analytically obtained ω_{max} is represented with vertical dashed lines. Shaded regions on all sub-figures represent the theoretical band gap ranges. (Online version in colour.)

be shown to be equal to the product of the off-diagonal elements of $\mathbf{D}(s)$, which, in our case, results in $Z(s) = \kappa^n/k_1$. The procedure of deriving the zeros polynomial explained earlier has been thoroughly discussed in Miu [46,47] and recently applied in the context of periodic structures by the authors [8,11,22]. As such, the details of these derivations are omitted here for brevity. Finally, the ratio of the zeros to the characteristic (poles) polynomials provides the sought end-to-end transfer function:

$$\frac{u_{\mathcal{Z}n}(s)}{f(s)} = \frac{Z(s)}{P(s)} = \frac{\kappa^n/k_1}{\Delta_{1,\mathcal{Z}}^* \prod_{\ell=1}^{n-1} \left(\sum_{\xi=1}^{\mathcal{Z}} \alpha_{\xi} s^{2\xi} + 2\kappa (1 - \cos(\theta_{\ell}))\right)}.$$
 (3.17)

(iii) Frequency response function

The frequency response function (FRF) of the different permutations of a finite triatomic lattice (shown in figure 2) is extracted from the transfer function in equation (3.17) by substituting $s = i\omega$. Figure 9 shows these FRFs for n = 10 (a) as well as the pole (i.e. natural frequencies) distribution projected on the dispersion curves (b). The results have been also validated by solving $\mathbf{u}(\omega) = \mathbf{D}(\omega)^{-1}\mathbf{f}(\omega)$ numerically. As expected, each group of cyclic permutations which share an identical dispersion relation exhibit the same band gap frequency range as well as the same set of natural frequencies obtained from the second term of equation (3.16). However, a key difference between the different cyclic permutations is the location of the truncation poles (i.e. poles that lie within the band gap range in this example) given instead by the roots of the term $\Delta_{1,\mathcal{Z}}^*$. The presence of a truncation pole represents a discontinuity within the finite PC's band gap which also alters the location (frequency) of the maximum attenuation point. This can be seen in the discrepancy between the numerically obtained maximum attenuation in the FRF (marked as circles in figure 9) and the analytically obtained ω_{max} (vertical dashed line in figure 9). Although $\omega = 0$ is a solution for $\Delta_{1,\mathcal{Z}}^*$, it cannot be considered as a truncation pole as it does not occur within a band gap, in addition to the fact that it satisfies the dispersion relation for $\bar{\beta} = 0$. Instead, $\omega = 0$ indicates a rigid

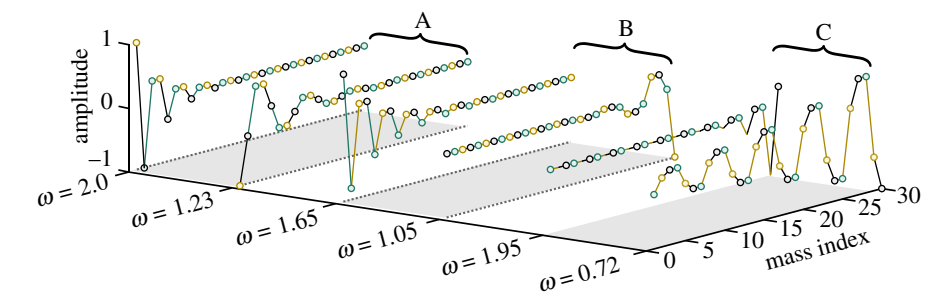


Figure 10. Mode shapes corresponding to truncation poles within the band gaps of figure 9 for cases A, B and C. (Online version in colour.)

body mode of the unconstrained lattice as a result of the free–free boundary conditions. In what follows, we elaborate on the behaviour of finite PCs at the truncation frequencies that manifest themselves within a band gap.

(c) Edge modes in polyatomic lattices

(i) Truncation poles and corresponding eigenmodes

The presence of a resonant frequency (pole) within a band gap of a finite PC is a byproduct of the truncation of the infinite structure [6]. Furthermore, the derived expression for $\Delta_{1,\mathbb{Z}}^*$ in equation (3.14) indicates that such truncation poles coincide with the poles of a single unconstrained unit cell. Mode shapes associated with truncation poles resemble a propagating wave with an exponential spatial decay profile starting from one end of the finite lattice. This is demonstrated in figure 10 for the three first permutations of the triatomic lattice (i.e. A through C). Note that a mode shape is a property of the dynamical system and does not change with different excitation locations. Thus, a triatomic PC with the configuration C, for example, will always have the mode shapes in figure 10 even if the excitation is imposed on the first mass (i.e. mass index = 1 in the figure). In the latter case, the wave can be therefore perceived as exponentially growing, instead of decaying, from the excitation point. Based on the behaviour of the mode shapes, several observations are made: (i) the spatial decay of the wave is rapid for poles that are closer to $\omega_{\rm max}$ of the respective band gap, (ii) large localized displacement may occur at either of the end masses regardless of the excitation location and (iii) the alike masses move out- or in-phase for the first and second truncation pole, respectively, validating the results in figure 5. These modes are reminiscent of edge modes in two-dimensional structures where a large localized displacement materializes on one of the system boundaries [48].

All the cases portrayed in figure 10 describe lattices with different masses and spring constants, simultaneously, in addition to the fact that all the permutations are cyclic. It is worth mentioning, however, that when the masses are equal, there exist non-cyclic permutations that have identical FRFs as well as natural frequencies (figure 3 as a case in point). An illustrative example of the latter is depicted in figure 11 for 1–2–3 and 1–3–2 permutations of the triatomic PC with equal masses $m_1 = m_2 = m_3 = 1$. Despite the matching responses, the two non-cyclic permutations clearly have distinct eigenvectors for a given truncation pole (shown in figure 11*b*). It can be also observed that these two eigenvectors are mirror images of each other. This type of modes has been recently exploited to create a unique topological behaviour in an array of coupled rods with quasi-periodic parameters [33].

(ii) Edge modes in mirror symmetric polyatomic phononic crystals

In the previous section, we discussed the truncation pole phenomenon for a general polyatomic PC (i.e. with both mass and stiffness variations) as a result of an arbitrary truncation of the infinite

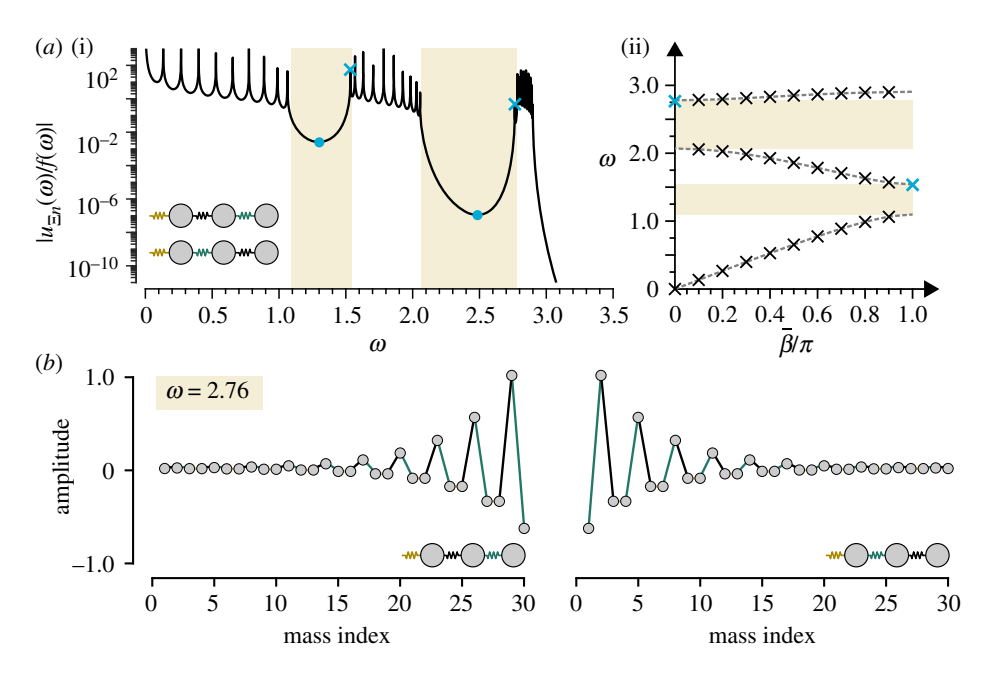


Figure 11. (a(i)) Frequency response function (FRF) of the 1–2–3 and 1–3–2 arrangements of a triatomic PC with identical masses. (a(ii)) Corresponding distribution of natural frequencies of the finite PC (marked as cross symbols) projected on the band structure obtained for an infinite system. Shaded regions in both figures represent the theoretical band gap ranges. (b) Mode shapes corresponding to the second truncation pole (i.e. $\omega = 2.76$) for both permutations. (Online version in colour.)

lattice. In the context of dispersion topology, such simultaneous mass and stiffness variations result in a non-integer winding number v. Thus, the conditions established in §§2f have to be met to ensure that a given truncation pole indeed corresponds to a non-trivial mode inside the band gap. If mirror symmetry is established in a polyatomic lattice with free-free boundary conditions, the truncation poles observed in §3c(i) disappear and move to the bulk mode. A test for whether or not a lattice supports an edge mode is to prescribe a fixed boundary condition at one end [34]. In here, we consider the tetratomic lattice in figure 8 to illustrate the creation of such an edge mode. We adopt the following parametrization for the springs: $k_1 = (k/5)(2-a)$, $k_3 = (k/5)(2+a)$ and $k_2 = (k/5)$ such that their summation is always equal to k, consistent with figure 8. Varying a closes the first and third band gaps at $a = \pm \sqrt{2}$ and the second band gap at a = 0. For each band gap closing/opening, an edge mode is observed in figure 12a, albeit not as flat (robust) as traditionally encountered in diatomic PCs [34]. However, unlike diatomic PCs with a single winding number for both dispersion branches, it remains more challenging to determine when an edge mode is supported in polyatomic lattices where each dispersion band exhibits a unique ν value. To resolve this, we assign a characteristic number ν_g to each band gap reminiscent of band gap Chern numbers [49,50], to better relate the behaviour of the finite lattice to information obtained earlier from the band topology. For a given gap, v_g is defined as the summation of the winding numbers of the bands beneath it and its value is indicated in figure 12b. Interestingly, we observe that the emergence of an edge mode happens only in conjunction with an odd v_g . To confirm this hypothesis, we simulate the finite system for all possible stiffness combinations in the same barycentric space and perform a binary search for the existence of an edge mode (1), or lack thereof (0). The binary map shown in figure 12c confirms the dispersion-based predictions and precisely matches it when the operation $mod(v_g, 2)$ is carried out. The 'red' region represents a small design space where the edge mode will not be supported for the current boundary condition choice (i.e. fixed-free). This is however remedied by shifting to a fixed-fixed lattice and this region is then recovered. Finally, figure 12d shows results when the same analysis is carried out for the pentatomic lattice in figure 8, which are fully consistent with the previous discussion.

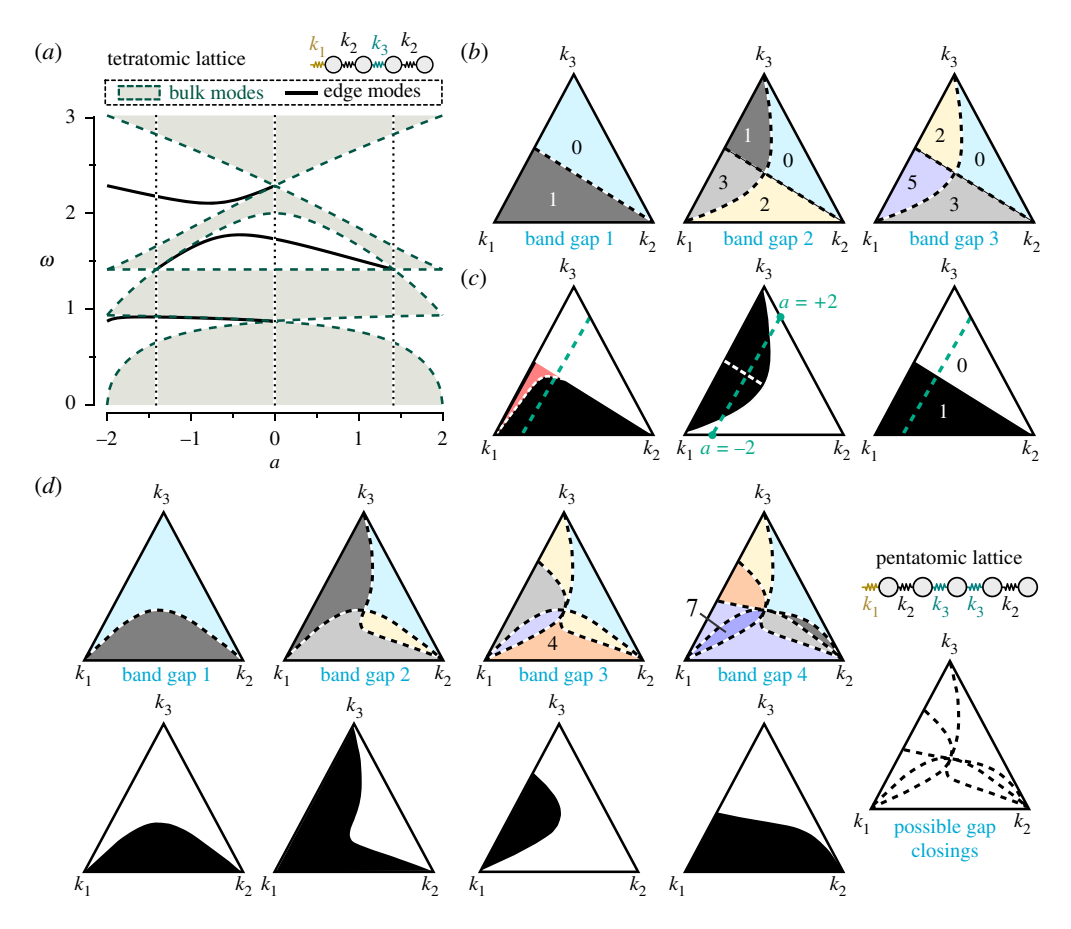


Figure 12. (a) Bulk and edge modes of a tetratomic lattice corresponding to a variation in the springs across the green dashed line in the barycentric space depicted in sub-figure (c). (b) Values of the characteristic number v_g for the three band gaps of the tetratomic lattice shown in figure 8. (c) A binary map indicating the support of an edge mode (1) or a lack thereof (0). (d) A replication of the same analysis on the pentatomic lattice. A unit cell of the latter is provided for reference. (Online version in colour.)

(iii) Truncation poles and two-dimensional lattices

The mode shapes of the truncation poles can be exploited to create an edge mode in a twodimensional lattice structure based on the one-dimensional model. In figure 13, we demonstrate a two-dimensional lattice built from an array of a one-dimensional triatomic PC with the permutation 1-2-3 (i.e. permutation A in figure 2) stacked in the y-direction and coupled with a relatively stiff spring k_y (here, we used $k_y/k_1 = 10^3$) similar to the system discussed in [33]. If the two-dimensional system is excited with a sine sweep at one corner and the response is measured from the opposing one, the resulting FRF is qualitatively analogous to that of the onedimensional model as seen in the frequency response in figure 13. In addition, the mode shape of the two-dimensional lattice (when seen from the front view) mimics that of its one-dimensional counterpart illustrated in figure 10. The ease of pinpointing edge modes frequencies by only considering the eigenvalue problem of a single unit cell facilitates their analysis and provides physical intuition into the relation of such modes with the constitutive unit cell. It is worth noting that the 2D mode presented here is not topologically protected and further considerations should be taken into account to ensure such protection. Examples of the latter include stacking and coupling a family of modulated one-dimensional lattices along a second spatial dimension [50], adiabatic spatio-temporal modulation of mechanical properties [51], as well as gyroscopic effects [52].

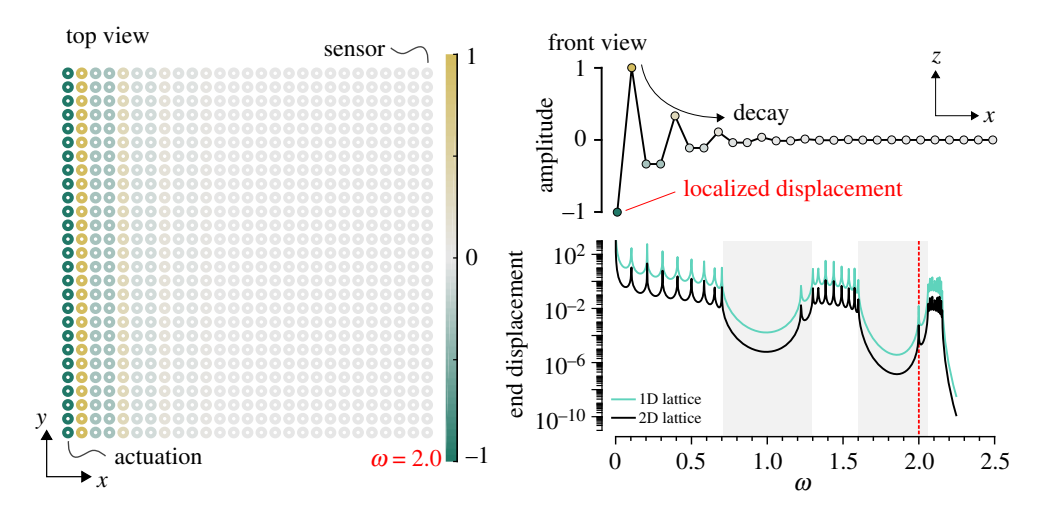


Figure 13. Edge mode in a two-dimensional polyatomic lattice built from an array of one-dimensional polyatomic PCs. The lattice is constructed from arrangement A in figure 2 coupled with stiff springs in the *y*-direction. The corresponding FRFs for the end displacement shows the qualitative similarities between the one- and two-dimensional cases. (Online version in colour.)

(d) Band gap formation mechanism

The formation mechanism of Bragg-type band gaps in finite lattices has been explained in light of the Bode plot analysis. Moreover, the strong dependence of band gap strength, width and location on the pole distribution has been thoroughly investigated for a finite diatomic PC [8]. In the latter, periodically placing two spring-mass systems with distinct properties splits the total set of natural frequencies into two groups on both sides of the sole band gap. These two groups of natural frequencies can be perceived as a low-frequency 'pass-band' FRF and a high-frequency one, respectively. Since a standard Bode plot is based on a log-log scale which automatically converts the multiplication of terms into addition, the superposition of these two FRFs returns the frequency response of the entire system. At the tail end of the low-frequency pass band, the FRF acts as a filter following its last pole due to the accumulated contribution of $-20\,\mathrm{dB/decade}$ per pole. The second high-frequency pass band puts an end to the attenuation of the low-frequency pass band and provides the upper bound of the band gap.

The analysis of the emergence of multiple band gaps in higher-order hierarchies is analogous to that of the diatomic lattice. Here, we establish a generalized procedure to physically interpret the formation mechanism of multiple band gaps using a systematic Bode plot analysis. We start by computing the roots of the characteristic polynomial P(s) in equation (3.16). For each value of θ_{ℓ} , Ξ positive solutions are found, each of which corresponds to one pass band. Once all the solutions are computed, they are sorted based on the number of the pass band, which will result in Ξ pole groups that can be mathematically presented as

$$\frac{u_{\mathcal{Z}n}(\omega)}{f(\omega)} = \frac{\kappa^n}{k_1 \prod_{\xi=1}^{\mathcal{Z}} m_{\xi}} \times \frac{1}{\prod_{q=1}^{n} (\omega^2 - \omega_q^2)} \times \frac{1}{\prod_{q=1}^{n} (\omega^2 - \omega_{q+n}^2)} \times \dots \times \frac{1}{\prod_{q=1}^{n} (\omega^2 - \omega_{q+(\mathcal{Z}-1)n}^2)}.$$
(3.18)

Taking the natural logarithm of equation (3.18) results in a summation series and the pole groups corresponding to each band can be now denoted by T_{ξ} , and mathematically written as

$$T_{\xi} = \sum_{q=1}^{n} \ln \left(\frac{1}{\omega^2 - \omega_{q+(\xi-1)n}^2} \right),$$
 (3.19)

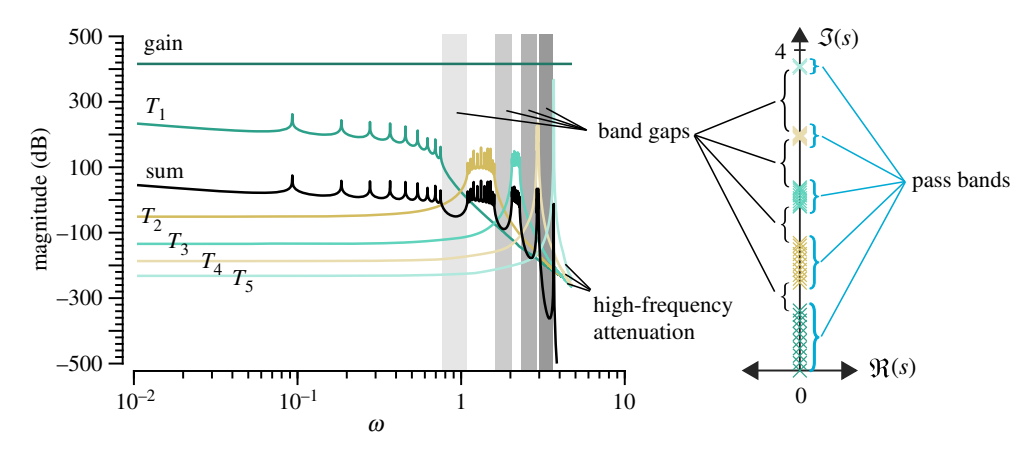


Figure 14. An illustration of multiple band gap formation in a pentatomic PC. The figure shows the individual Bode plots for the five transfer functions (T_1 through T_5) extracted from equation (3.19). The transfer functions contain the entire system poles distributed across five pass bands as shown on the right. The global transfer function is the summation of T_1 through T_5 in addition to the gain T_0 . Band gap regions are shaded on the Bode plot and marked on the pole map. (Online version in colour.)

with the gain being

$$T_0 = \ln\left(\frac{\varkappa^n}{k_1 \prod_{\xi=1}^{\Xi} m_{\xi}}\right). \tag{3.20}$$

We conclude with an illustrative visual presentation of the formation mechanism for a pentatomic PC in figure 14. If each of the T_{ξ} terms is plotted separately, we notice that the first group of poles in T_1 acts as a *low-pass filter*. The remaining transfer functions, however, behave as pass-band filters. The pass-band filters allow waves to pass within their respective frequency ranges and, otherwise, attenuate them. This is confirmed by the behaviour of the transfer function T_{ξ} for $\xi > 1$. It is also evident in figure 14 that the contribution of the poles of T_{ξ} ($\xi > 1$) is negligible at lower frequencies, while the collective high-frequency attenuation by the poles kicks in once the frequency hits the last pole of the group. As such, the band gap formation is effectively a collective contribution of the attenuation regions of a series of multiple pass-band filters. The decrease in the amplitude of a group of poles, say the ξ th group, is compensated with the increase in the amplitude caused by the $(\xi + 1)$ th group and the maximum attenuation occurs relatively midway between the last pole of ξ th group and the first pole of the $(\xi + 1)$ th group. Each separating region between two pass-band filters is equivalent to one of the band gaps predicted by the traditional wave dispersion analysis. It is also important to point out that higher-order band gaps enjoy steeper magnitude reduction in the FRF as a direct consequence of the larger collective high-frequency attenuation of the increasing number of poles. This is perfectly in line with the attenuation constants (imaginary component of $\bar{\beta}$) shown in dispersion diagrams in figures 2 and 3. Finally, it can also be observed that the pass-band regions tend to have a higher Q-factor at higher frequencies. The framework presented here to quantify the formation of band gaps in finite periodic systems is general and extendable to higher-order polyatomic phononic lattices as well as continuous phononic structures.

4. Concluding remarks

This paper has established a rigorous mathematical framework to quantify: (1) wave dispersion and topological characteristics and (2) finite structural dynamics of a generalized polyatomic phononic crystal (PC) comprising, in its general form, a series of two or more arbitrarily arranged monatoms. The governing dispersion relation has been derived in closed-form for any given number of monatomic subcells constituting the polyatomic unit cell. Different characteristics of the dispersion relation including the sonic speed and maximum attenuation within band gaps

have been outlined. The different effects of changing the atomic arrangements of the individual subcells, as well as conditions leading to identical and distinct band structures have been shown. The resultant topological aspects associated with different cellular permutations of the polyatomic PCs have been quantified via the winding number of the complex eigenvector and shown to be quantized in the presence of mirror symmetry. It has been also established that the emergence of an edge mode is sensitive to the parity of the characteristic metric v_g , and materializes only at odd values of it. A generalized form of the end-to-end transfer function of any polyatomic PC was also obtained and several examples were presented to highlight the natural frequency (pole) distribution of the finite lattice and its correlation to the infinite dispersion predictions. An interpretation of truncation modes which appear inside the band gaps of a free–free polyatomic lattice has been provided, as well as a brief discussion of how such modes can be potentially exploited to realize edge states in two-dimensional lattices. Finally, a generalized theorem to interpret the evolution and formation mechanism of multiple Bragg-type band gaps in finite polyatomic PCs has been provided based on the Bode plot analysis.

Competing interests. The authors declare no competing interest.

Data accessibility. All the data are included in the manuscript.

Authors' contributions. T.S. proposed the Bode plot analysis and the band gap formation mechanism in finite phononic lattices. H.A. conceived the mathematical framework, and performed derivations and simulations for the dispersion relation characteristics of cellular permutations, topological aspects, eigenvalues and mode shapes, as well as the end-to-end transfer function. H.A., M.N. and T.S. designed the research and analysed the results. H.A. and M.N. co-wrote the paper.

Funding. The authors acknowledge the support of this work from the US National Science Foundation via CMMI grant no. 1647744.

References

- 1. Wang G, Yu D, Wen J, Liu Y, Wen X. 2004 One-dimensional phononic crystals with locally resonant structures. *Phys. Lett. A* **327**, 512–521. (doi:10.1016/j.physleta.2004.05.047)
- 2. Krushynska AO, Miniaci M, Kouznetsova VG, Geers MG. 2017 Multilayered inclusions in locally resonant metamaterials: two-dimensional versus three-dimensional modeling. *J. Vib. Acoust.* **139**, 024501. (doi:10.1115/1.4035307)
- 3. Wang Y, Wang Y. 2013 Complete bandgaps in two-dimensional phononic crystal slabs with resonators. *J. Appl. Phys.* **114**, 043509. (doi:10.1063/1.4816273)
- 4. Deymier PA. 2013 *Acoustic metamaterials and phononic crystals*. Springer Series in Solid-State Sciences, vol. 173. Berlin, Germany: Springer Science.
- 5. Yang S, Page JH, Liu Z, Cowan ML, Chan CT, Sheng P. 2004 Focusing of sound in a 3D phononic crystal. *Phys. Rev. Lett.* **93**, 024301. (doi:10.1103/PhysRevLett.93.024301)
- 6. Hussein M, Biringen S, Bilal O, Kucala A. 2015 Flow stabilization by subsurface phonons. *Proc. R. Soc. A* **471**, 20140928. (doi:10.1098/rspa.2014.0928)
- 7. Peng YG, Qin CZ, Zhao DG, Shen Y-X, Xu XY, Bao M, Jia H, Zhu X-F. 2016 Experimental demonstration of anomalous Floquet topological insulator for sound. *Nat. Commun.* 7, 13368. (doi:10.1038/ncomms13368)
- 8. Al Ba'ba'a H, Nouh M, Singh T. 2017 Pole distribution in finite phononic crystals: understanding Bragg-effects through closed-form system dynamics. *J. Acoust. Soc. Am.* **142**, 1399–1412. (doi:10.1121/1.5001513)
- 9. Sugino C, Leadenham S, Ruzzene M, Erturk A. 2016 On the mechanism of bandgap formation in locally resonant finite elastic metamaterials. *J. Appl. Phys.* **120**, 134501. (doi:10.1063/1.4963648)
- 10. Yilmaz C, Hulbert G. 2010 Theory of phononic gaps induced by inertial amplification in finite structures. *Phys. Lett. A* **374**, 3576–3584. (doi:10.1016/j.physleta.2010.07.001)
- 11. Al Ba'ba'a H, DePauw D, Singh T, Nouh M. 2018 Dispersion transitions and pole-zero characteristics of finite inertially amplified acoustic metamaterials. *J. Appl. Phys.* **123**, 105106. (doi:10.1063/1.5019703)
- 12. Chen Y, Huang G, Sun C. 2014 Band gap control in an active elastic metamaterial with negative capacitance piezoelectric shunting. *J. Vib. Acoust.* **136**, 061008. (doi:10.1115/1.4028378)

- 13. Hussein MI, Leamy MJ, Ruzzene M. 2014 Dynamics of phononic materials and structures: historical origins, recent progress, and future outlook. *Appl. Mech. Rev.* **66**, 040802. (doi:10.1115/1.4026911)
- 14. Narisetti R, Ruzzene M, Leamy M. 2011 A perturbation approach for analyzing dispersion and group velocities in two-dimensional nonlinear periodic lattices. *J. Vib. Acoust.* **133**, 061020. (doi:10.1115/1.4004661)
- 15. Narisetti RK, Leamy MJ, Ruzzene M. 2010 A perturbation approach for predicting wave propagation in one-dimensional nonlinear periodic structures. *J. Vib. Acoust.* **132**, 031001. (doi:10.1115/1.4000775)
- 16. Ganesh R, Gonella S. 2015 From modal mixing to tunable functional switches in nonlinear phononic crystals. *Phys. Rev. Lett.* **114**, 054302. (doi:10.1103/PhysRevLett.114.054302)
- 17. Porubov A, Andrianov I. 2013 Nonlinear waves in diatomic crystals. *Wave Motion* **50**, 1153–1160. (doi:10.1016/j.wavemoti.2013.03.009)
- 18. Pal RK, Vila J, Leamy M, Ruzzene M. 2018 Amplitude-dependent topological edge states in nonlinear phononic lattices. *Phys. Rev. E* **97**, 032209. (doi:10.1103/PhysRevE.97.032209)
- 19. Vila J, Pal RK, Ruzzene M, Trainiti G. 2017 A bloch-based procedure for dispersion analysis of lattices with periodic time-varying properties. *J. Sound Vib.* **406**, 363–377. (doi:10.1016/j.jsv.2017.06.011)
- 20. Attarzadeh M, Al Ba'ba'a H, Nouh M. 2018 On the wave dispersion and non-reciprocal power flow in space-time traveling acoustic metamaterials. *Appl. Acoust.* **133**, 210–214. (doi:10.1016/j.apacoust.2017.12.028)
- 21. Hussein MI. 2009 Reduced Bloch mode expansion for periodic media band structure calculations. *Proc. R. Soc. A* 465, 2825–2848. (doi:10.1098/rspa.2008.0471)
- 22. Al Ba'ba'a H, Nouh M, Singh T. 2017 Formation of local resonance band gaps in finite acoustic metamaterials: a closed-form transfer function model. *J. Sound Vib.* 410, 429–446. (doi:10.1016/j.isv.2017.08.009)
- 23. Hvatov A, Sorokin S. 2015 Free vibrations of finite periodic structures in passand stop-bands of the counterpart infinite waveguides. *J. Sound Vib.* **347**, 200–217. (doi:10.1016/j.jsv.2015.03.003)
- 24. Nielsen R, Sorokin S. 2015 Periodicity effects of axial waves in elastic compound rods. *J. Sound Vib.* **353**, 135–149. (doi:10.1016/j.jsv.2015.05.013)
- 25. Shen X, Sun C, Barnhart M, Huang G. 2018 Analysis of dynamic behavior of the finite elastic metamaterial-based structure with frequency-dependent properties. *J. Vib. Acoust.* **140**, 031012. (doi:10.1115/1.4038950)
- 26. Cheng Z-B, Lin W-K, Shi Z-F. 2017 Dispersion differences and consistency of artificial periodic structures. *IEEE Trans. Ultrason. Ferroelectr. Freq. Control* **64**, 1591–1598. (doi:10.1109/TUFFC.2017.2725942)
- 27. Cheng Z-B, Shi Z-F. 2014 Multi-mass-spring model and energy transmission of one-dimensional periodic structures. *IEEE Trans. Ultrason. Ferroelectr. Freq. Control* **61**, 739–746. (doi:10.1109/TUFFC.2014.2966)
- 28. Michelitsch T, Collet B. 2014 A nonlocal constitutive model generated by matrix functions for polyatomic periodic linear chains. *Arch. Appl. Mech.* **84**, 1477–1500. (doi:10.1007/s00419-014-0905-3)
- 29. Xiong L, Chen X, Zhang N, McDowell DL, Chen Y. 2014 Prediction of phonon properties of 1D polyatomic systems using concurrent atomistic–continuum simulation. *Arch. Appl. Mech.* **84**, 1665–1675. (doi:10.1007/s00419-014-0880-8)
- 30. Haque AT, Ghachi RF, Alnahhal WI, Aref A, Shim J. 2018 Sagittal plane waves in infinitely periodic multilayered composites composed of alternating viscoelastic and elastic solids. *J. Appl. Mech.* **85**, 041001. (doi:10.1115/1.4039039)
- 31. Rózsa P. 1969 On periodic continuants. *Linear Algebra Appl.* **2**, 267–274. (doi:10.1016/0024-3795(69)90030-5)
- 32. Pal RK, Ruzzene M. 2017 Edge waves in plates with resonators: an elastic analogue of the quantum valley hall effect. *New J. Phys.* **19**, 025001. (doi:10.1088/1367-2630/aa56a2)
- 33. Rosa MI, Pal RK, Arruda JR, Ruzzene M. 2018 Boundary modes in quasiperiodic elastic structures. In *Behavior and mechanics of multifunctional materials and composites XII* (ed. HE Naguib), vol. 10596, p. 1059606. Bellingham, WA: International Society for Optics and Photonics.
- 34. Chen H, Nassar H, Huang G. 2018 A study of topological effects in 1d and 2d mechanical lattices. *J. Mech. Phys. Solids* 117, 22–36. (doi:10.1016/j.jmps.2018.04.013)

- 35. Kouachi S. 2006 Eigenvalues and eigenvectors of tridiagonal matrices. *Electron. J. Linear Algebra* **15**, 8. (doi:10.13001/1081-3810.1223)
- 36. Kouachi S. 2008 Eigenvalues and eigenvectors of some tridiagonal matrices with non-constant diagonal entries. *Applicationes Mathematicae* **35**, 107–120. (doi:10.4064/am35-1-7)
- 37. da Fonseca C. 2007 The characteristic polynomial of some perturbed tridiagonal k-toeplitz matrices. *Appl. Math. Sci* **1**, 59–67.
- 38. Basin S. 1964 An application of continuants. *Math. Mag.* **37**, 83–91. (doi:10.1080/0025570X.1964.11975488)
- 39. Hussein MI, Frazier MJ. 2013 Metadamping: an emergent phenomenon in dissipative metamaterials. *J. Sound Vib.* **332**, 4767–4774. (doi:10.1016/j.jsv.2013.04.041)
- 40. Xiao M, Ma G, Yang Z, Sheng P, Zhang Z, Chan CT. 2015 Geometric phase and band inversion in periodic acoustic systems. *Nat. Phys.* **11**, 240–244. (doi:10.1038/nphys3228)
- 41. He C, Ni X, Ge H, Sun X-C, Chen Y-B, Lu M-H, Liu X-P, Chen Y-F. 2016 Acoustic topological insulator and robust one-way sound transport. *Nat. Phys.* **12**, 1124–1129. (doi:10.1038/nphys3867)
- 42. Hensley D. 2006 Continued fractions, vol. 20. Singapore: World Scientific.
- 43. Zak J. 1989 Berry's phase for energy bands in solids. *Phys. Rev. Lett.* **62**, 2747. (doi:10.1103/PhysRevLett.62.2747)
- 44. Delplace P, Ullmo D, Montambaux G. 2011 Zak phase and the existence of edge states in graphene. *Phys. Rev. B* 84, 195452. (doi:10.1103/PhysRevB.84.195452)
- 45. Marques A, Dias R. 2017 Generalization of Zak's phase for lattice models with non-centered inversion symmetry axis. (http://arxiv.org/abs/1707.06162).
- 46. Miu D. 1993 Mechatronics: electromechanics and contromechanics. New York, NY: Springer.
- 47. Miu DK. 1991 Physical interpretation of transfer function zeros for simple control systems with mechanical flexibilities. *J. Dyn. Syst., Meas. Control* 113, 419–424. (doi:10.1115/1.2896426)
- 48. Kraus YE, Lahini Y, Ringel Z, Verbin M, Zilberberg O. 2012 Topological states and adiabatic pumping in quasicrystals. *Phys. Rev. Lett.* **109**, 106402. (doi:10.1103/PhysRevLett.109.106402)
- 49. Chaunsali R, Li F, Yang J. 2016 Stress wave isolation by purely mechanical topological phononic crystals. *Sci. Rep.* **6**, 30662. (doi:10.1038/srep30662)
- 50. Rosa MI, Pal RK, Arruda JR, Ruzzene M. 2018 Edge states and topological pumping in elastic lattices with periodically modulated coupling. (http://arxiv.org/abs/1811.02637).
- 51. Attarzadeh M, Nouh M. 2018 Non-reciprocal elastic wave propagation in 2D phononic membranes with spatiotemporally varying material properties. *J. Sound Vib.* **422**, 264–277. (doi:10.1016/j.jsv.2018.02.028)
- 52. Wang P, Lu L, Bertoldi K. 2015 Topological phononic crystals with one-way elastic edge waves. *Phys. Rev. Lett.* **115**, 104302. (doi:10.1103/PhysRevLett.115.104302)